Author Manuscript

Author Manuscript

Author Manuscript

Author Manuscript

HHS Public Access

Author manuscript

Nat Med. Author manuscript; available in PMC 2021 March 30.

Published in final edited form as:

Nat Med. 2020 September ; 26(9): 1444–1451. doi:10.1038/s41591-020-0986-1.

Therapeutic efficacy of antisense oligonucleotides in mouse models of CLN3 Batten disease

Jessica L. Centa[1,2], **Francine M. Jodelka**[1], **Anthony J. Hinrich**[1], **Tyler B. Johnson**[3], **Joseph Ochaba**[4], **Michaela Jackson**[4], **Dominik M. Duelli**[5], **Jill M. Weimer**[3,6], **Frank Rigo**[4], **Michelle L. Hastings**[1,2,✉]

[1]Center for Genetic Diseases, Chicago Medical School, Rosalind Franklin University of Medicine and Science, North Chicago, IL, USA.

[2]School of Graduate and Postdoctoral Studies, Rosalind Franklin University of Medicine and Science, North Chicago, IL, USA.

[3]Pediatrics and Rare Diseases Group, Sanford Research, Sioux Falls, SD, USA.

[4]Ionis Pharmaceuticals, Carlsbad, CA, USA.

[5]Cellular and Molecular Pharmacology, Chicago Medical School, Rosalind Franklin University of Medicine and Science, North Chicago, IL, USA.

[6]Department of Pediatrics, Sanford School of Medicine, University of South Dakota, Sioux Falls, SD, USA.

Abstract

CLN3 Batten disease is an autosomal recessive, neurodegenerative, lysosomal storage disease caused by mutations in *CLN3*, which encodes a lysosomal membrane protein[1–3]. There are no disease-modifying treatments for this disease that affects up to 1 in 25,000 births, has an onset of symptoms in early childhood and typically is fatal by 20–30 years of life[4–7]. Most patients with CLN3 Batten have a deletion encompassing exons 7 and 8 (*CLN3*$^{\Delta ex7/8}$), creating a reading frame-shift[7,8]. Here we demonstrate that mice with this deletion can be effectively treated using an

✉**Correspondence and requests for materials** should be addressed to M.L.H. michelle.hastings@rosalindfranklin.edu.

Author contributions

J.L.C., F.M.J. and M.L.H. designed and carried out mouse behavioral analysis; J.L.C., A.J.H. and M.L.H. designed and performed *in vitro* ASO experiments; J.L.C. and A.J.H. performed immunofluorescent analysis of ASO distribution; T.B.J and J.M.W. carried out immunohistochemistry for SCMAS accumulation and GFAP; J.O. and F.R. designed, performed and analyzed data from experiments to measure autophagy and lysosomal volume; M.J. and F.R. designed and performed adult ICV treatments. J.M.W., F.R., D.M.D and M.L.H. provided critical materials and reagents. J.L.C. and M.L.H. wrote the manuscript. All authors discussed the results and contributed to the preparation of the manuscript.

Competing interests

J.O, M.J. and F.R. are employees of Ionis Pharmaceuticals. T.B.J. and J.M.W. are currently employees of Amicus Therapeutics. D.M.D. is currently employed by Abbott Molecular. M.L.H. and F.R. are inventors on patents on ASOs filed by RFUMS and Ionis Pharmaceuticals and may be entitled to benefits from licensing of the associated intellectual property.

Additional information

Extended data is available for this paper at https://doi.org/10.1038/s41591-020-0986-1.

Supplementary information is available for this paper at https://doi.org/10.1038/s41591-020-0986-1.

Peer review information Kate Gao was the primary editor on this article and managed its editorial process and peer review in collaboration with the rest of the editorial team.

Reprints and permissions information is available at www.nature.com/reprints.

Author Manuscript Author Manuscript Author Manuscript Author Manuscript

antisense oligonucleotide (ASO) that induces exon skipping to restore the open reading frame. A single treatment of neonatal mice with an exon 5-targeted ASO-induced robust exon skipping for more than a year, improved motor coordination, reduced histopathology in *Cln3*$^{\Delta ex7/8}$ mice and increased survival in a new mouse model of the disease. ASOs also induced exon skipping in cell lines derived from patients with CLN3 Batten disease. Our findings demonstrate the utility of ASO-based reading-frame correction as an approach to treat CLN3 Batten disease and broaden the therapeutic landscape for ASOs in the treatment of other diseases using a similar strategy.

The deletion of exons 7 and 8, the most common mutation associated with CLN3 Batten disease, results in a premature termination codon in exon 9 of the 15-exon gene (Fig. 1a). The resulting protein, CLN3$^{\Delta ex7/8}$, encodes a 181 amino acid (aa) peptide lacking the 257 aa at the C-terminus of the wild-type (WT) CLN3 protein that includes the lysosomal targeting sequence (LTS)[1]. We reasoned that correcting the reading frame of *CLN3*$^{\Delta ex7/8}$ by deleting exon 5 to produce *CLN3* mRNA lacking exons 5, 7 and 8 (*CLN3*$^{\Delta ex5/7/8}$) would partially compensate for loss of CLN3 by restoring the C-terminal portion of the protein, thereby providing therapeutic value for CLN3 Batten disease. The function of CLN3 is unclear and there is limited information about the structure of CLN3 in the lysosomal membrane to help predict activity of CLN3$^{\Delta ex5/7/8}$. CLN3 structural modeling provides a consensus model with 11 transmembrane domains (TMDs), and five TMDs for CLN3$^{\Delta ex5/7/8}$ with the N- and C-termini conserved (Extended Data Fig. 1). CLN3$^{\Delta ex7/8}$ is predicted to have three TMDs with a novel C-terminus. Some additional rationale to support a reading-frame correction approach to treat CLN3 Batten comes from the spectrum of disease severity associated with different mutations in patients. Most cases of CLN3 Batten disease that are not exons 7/8 deletions are frame-shifting deletions and nonsense mutations that eliminate the LTS[9]. Rare missense mutations that do not disrupt the C-terminal LTS are associated with protracted disease[9,10] (NCL Mutation Database: http://www.ucl.ac.uk/ncl), consistent with the hypothesis that in-frame deletions may be better tolerated than truncations, which invariably cause severe forms of the disease.

Changes in lysosomal size and autophagic flux, involving the degradation and recycling of cellular components via autophagosome–lysosome fusion, have been associated with the pathophysiology of CLN3 Batten disease[11–15]. Previous studies have reported autophagy defects in patient-derived *CLN3*$^{\Delta ex7/8}$ cells and in WT cells expressing CLN3$^{\Delta ex7/8}$ (refs. [11–14]). As a first test of CLN3$^{\Delta ex5/7/8}$ activity, we assessed whether its expression altered autophagy. Using a dual-labeled sensor to quantify autophagosomes and autophagic flux[12,16], we found that overexpression of CLN3$^{\Delta ex7/8}$ resulted in a significant increase in autophagic vesicles, which was not observed with overexpression of WT or CLN3$^{\Delta ex5/7/8}$ (Fig. 1b and Extended Data Fig. 2a,b). The number of LAMP1-positive vesicles (lysosomes) per cell was not different between cells that expressed the different proteins but there was an increase in vesicle volume with CLN3$^{\Delta ex7/8}$ overexpression that was not observed with WT or CLN3$^{\Delta ex5/7/8}$ expression (Fig. 1c and Extended Data Fig. 3a,b). Following autophagy induction with the mTORC1/2 inhibitor, AZD8055, CLN3- and CLN3$^{\Delta ex5/7/8}$-expressing cells showed a decrease in the ratio of autophagosomes to total autophagic vesicles, suggesting normal induction of autophagy and an increase in autophagic flux (Fig. 1d). By contrast, CLN3$^{\Delta ex7/8}$ cells showed an increase in autophagosomes relative to total

Author Manuscript Author Manuscript Author Manuscript Author Manuscript

autophagic vesicles, which is indicative of anomalous autophagic flux (Fig. 1d). During autophagy, LC3B-I is converted to LC3B-II and associates with the autophagosome, which matures and fuses with lysosomes to form the autolysosome where protein degradation, including that of LC3B-II and other cargo such as p62 (SQSTM1), occurs[17] (Extended Data Fig. 4a). We assessed LC3B dynamics during starvation-induced autophagy and found that LC3B-II and p62 were elevated in CLN3$^{\Delta ex7/8}$ cells compared to WT and CLN3$^{\Delta ex5/7/8}$-expressing cells, which is indicative of a defect in autophagic flux (Fig. 1e and Extended Data Fig. 4b,c). These results suggest that, unlike CLN3$^{\Delta ex7/8}$, expression of CLN3$^{\Delta ex5/7/8}$ is not associated with defects in autophagy.

With support for the hypothesis that conversion of CLN3$^{\Delta ex7/8}$ to CLN3$^{\Delta ex5/7/8}$ alleviates cellular deficits associated with the mutation, we developed an ASO-based approach to induce CLN3$^{\Delta ex5/7/8}$ expression. ASOs are a powerful therapeutic tool for facilitating specific, long-lasting changes in gene expression in vivo[18]. Splice-switching ASOs base-pair to the target pre-mRNA and alter splicing through steric hindrance[18]. We designed a series of 18-mer ASOs that base-pair in the exon 5 region (Fig. 1f). ASOs were transfected into a heterozygous *CLN3*$^{+/\Delta ex7/8}$ human fibroblast cell line and RNA was analyzed by PCR with reverse transcription (RT–PCR) (Fig. 1g). Most ASOs induced skipping of exon 5. The highly active ASO-20 and ASO-28 base-pair to the middle of the exon and across the 5′ splice site, respectively, and induced dose-dependent exon skipping (Fig. 1h and Extended Data Fig. 5a,b). The ASOs also induced robust exon 5 skipping in cell lines derived from multiple patients with homozygous *CLN3*$^{\Delta ex7/8}$ Batten disease (Fig. 1i and Extended Data Fig. 5c,d). There was an overall increase in *CLN3*$^{\Delta ex7/8}$-derived mRNA abundance upon ASO-mediated exon 5 skipping, which suggests that *CLN3*$^{\Delta ex7/8}$ mRNA is unstable, probably due to nonsense-mediated decay (NMD). Indeed, treating *CLN3*$^{\Delta ex7/8}$ human fibroblast cells with puromycin to inhibit NMD nearly doubled the abundance of the *CLN3*$^{\Delta ex7/8}$ mRNA (Extended Data Fig. 6a,b). ASO-induction of *CLN3*$^{\Delta ex5/7/8}$ resulted in an overall increase in both forms of *CLN3* mRNA, which was not as dramatically affected by puromycin treatment, which demonstrates that *CLN3*$^{\Delta ex5/7/8}$, the predominant isoform following ASO-treatment, is more stable than *CLN3*$^{\Delta ex7/8}$ (Extended Data Fig. 6a,b).

To test whether ASO-induced conversion of CLN3$^{\Delta ex7/8}$ to CLN3$^{\Delta ex5/7/8}$ can reverse aberrant autophagy associated with CLN3 Batten cells, we quantified LC3B in *CLN3*$^{+/\Delta ex7/8}$ heterozygous and homozygous *CLN3*$^{\Delta ex7/8}$ fibroblast cell lines. LC3B-II levels were reduced in cell lines derived from patients homozygous for *CLN3*$^{\Delta ex7/8}$ compared to cell lines derived from heterozygous controls in the basal state, in a similar manner to that reported previously[14] and also following treatment with AZD8055. Relative LC3B-II levels were partially restored to heterozygote levels by treatment of *CLN3*$^{\Delta ex7/8}$ patient cell lines with ASO-28 (Extended Data Fig. 4d–f), which suggests that ASO-mediated exon 5 skipping of *CLN3*$^{\Delta ex7/8}$ may normalize autophagic defects in the cells.

To test whether ASO-mediated exon 5 skipping can be achieved in vivo and provide therapeutic support in a mouse model of the disease, we tested ASOs that targeted murine exon 5 (Fig. 2a). ASOs were transfected into cell lines derived from a homozygous *Cln3*$^{\Delta ex7/8}$ mouse and splicing was analyzed by RT–PCR (Fig. 2b). ASO-26 was the most active and induced exon 5 skipping in a dose-dependent manner (Extended Data Fig. 7a,b).

Author Manuscript Author Manuscript Author Manuscript Author Manuscript

The most active ASOs were tested in mice with a deletion of *Cln3* exons 7 and 8 (*Cln3*$^{\Delta ex7/8}$)[19]. We delivered ASOs directly to the central nervous system (CNS) by intracerebroventricular (ICV) injection. ASO-26 was the most active ASO in adult heterozygous *Cln3*$^{+/\Delta ex7/8}$ mice two weeks after treatment (Fig. 2c). To assess the effect of ASO-induced exon 5 skipping on disease-associated outcomes, we treated neonatal mice to maximize the opportunity for prophylactic treatment prior to onset of symptoms and pathology[19]. Heterozygous and homozygous (*Cln3*$^{\Delta ex7/8/\Delta ex7/8}$) mice were treated at postnatal day 1 or 2 (P1–2) by ICV injection of ASO-26 or a control ASO (ASO-C), with no endogenous target. Treatment had no overt adverse effects on mouse health as assessed by weight and appearance (Extended Data Fig. 8a,b). Three weeks after treatment, tissue and RNA were collected and ASO distribution and exon 5 skipping were assessed. The ASO was distributed throughout the brain (Fig. 2d,e) and correlated with ASO exon 5 skipping activity throughout the CNS (Extended Data Fig. 9a,b). Analysis of splicing in the hippocampus at different time points after treatment revealed robust, stable exon 5 skipping for up to 14 months, which demonstrates long-term maintenance of ASOs in the CNS (Fig. 2f,g).

Patients with CLN3 Batten disease have accumulation of storage material made up predominantly of subunit c of mitochondrial ATP synthase (SCMAS)[20]. Homozygous *Cln3*$^{\Delta ex7/8}$ mice also accumulate SCMAS, exhibit glial activation throughout the CNS and have behavioral deficits[21–23]. ASO-26 treatment lowered SCMAS accumulation in the cortex, thalamus, striatum, and to a lesser extent, the hippocampus of homozygous *Cln3*$^{\Delta ex7/8}$ mice (Fig. 3a,b). *Cln3*$^{\Delta ex7/8/\Delta ex7/8}$ mice also have elevated glial fibrillary acidic protein (GFAP) immunoreactivity, which was reduced in the somatosensory cortex, striatum and thalamus of ASO-26-treated *Cln3*$^{\Delta ex7/8/\Delta ex7/8}$ mice compared to those treated with ASO-C (Fig. 3c,d). In the hippocampus, *Cln3*$^{\Delta ex7/8/\Delta ex7/8}$ mice have reduced GFAP, as previously reported[24], which was restored to heterozygous levels by ASO-26 treatment (Fig. 3c,d).

Motor deficits in homozygous *Cln3*$^{\Delta ex7/8}$ mice can be assessed by time spent on an accelerating rotarod and the ability to turn around on a vertical pole[21,25,26]. Two-month-old *Cln3*$^{+/\Delta ex7/8}$ mice performed significantly better on the tasks than did homozygous *Cln3*$^{\Delta ex7/8}$ mice and treatment of the mice with ASO-26 resulted in a significant improvement in performance compared to those treated with ASO-C. ASO-26-treated homozygous *Cln3*$^{\Delta ex7/8}$ mice were not significantly different than *Cln3*$^{+/\Delta ex7/8}$ mice in either task, which indicates a complete rescue of ability in these tasks (Fig. 4a,b).

Unlike those in human disease, *Cln3* mutations in mice do not cause early lethality[19]. The mouse brain may lack features of the human brain that make it less dependent on CLN3 for normal function. Incorporating additional burdens in the mouse brain, in particular on the lysosome and autophagy pathway, may result in a more severe response to *CLN3* mutations. Familial Alzheimer's disease (FAD) is an early onset form of the disease that can be caused by mutations in the amyloid precursor protein (APP). APP is an integral membrane protein that undergoes post-translational modifications and proteolytic cleavage events, some of which occur in the lysosome[27]. In mice, introduction of the human *APP* gene (*hAPP*) with FAD mutations results in an increase in proteolytic processing of APP and accumulation of amyloid beta (Aβ) peptides, which can accelerate neurodegeneration caused by impaired

Author Manuscript Author Manuscript Author Manuscript Author Manuscript

autophagy[28,29]. Aβ peptides have also been observed in the brains of patients with CLN3 Batten disease[30,31], suggesting that CLN3 depletion may result in accumulation of Aβ. In a similar manner, lipofuscins, such as those that accumulate in the tissues of patients with CLN3 Batten disease, are found in brain tissue from patients with FAD and idiopathic AD[32]. Expression of human APP with FAD alterations in a mouse model of another lysosomal storage disease, Niemann-Pick type C, worsens disease pathology, further linking aberrant APP with exacerbated lysosomal dysfunction[33]. These links between AD and lysosomal storage diseases, support a hypothesis that the expression of mutant human APP in mice will worsen disease symptomology of *Cln3*$^{\Delta ex7/8}$ mice. Thus, we crossed mice containing the FAD *hAPP* transgene[34] with *Cln3*$^{\Delta ex7/8}$ mice and treated them with ASO-C or ASO-26. Homozygous *Cln3*$^{\Delta ex7/8}$ mice with the FAD *hAPP* transgene had a 50% survival rate of 18.5 d. Treatment with ASO-26 resulted in significant improvement in survival, which was similar to the levels of survival observed in heterozygous *Cln3*$^{\Delta ex7/8}$ mice (Fig. 4c), providing evidence that this new exacerbated model of CLN3 Batten disease can be treated with ASO-26 to increase survival.

Here we demonstrate that a splice-switching ASO that targets the common CLN3 Batten disease mutation can ameliorate the effects of the disease in mice, demonstrating that ASO-mediated reading-frame correction can treat a lysosomal storage disease. We propose that the stabilization of the mRNA via elimination of the premature termination codon and the restoration of the C-terminus of the protein contribute to the therapeutic effect achieved by ASO-induced reading-frame correction.

ASO-based therapies are in the clinic as human disease treatments and many more are in development. ASOs do not efficiently cross the blood brain barrier, although treatment of the pediatric neurodegenerative disease spinal muscular atrophy (SMA) with ASOs is achieved by intrathecal administration, which is well tolerated[35]. Splice-switching ASOs have also been developed for the treatment of Duchenne muscular dystrophy to induce skipping of exons and correct the reading frame by eliminating mutations that create premature termination codons, similar to the strategy employed here[36].

Most ASOs we tested induced robust exon 5 skipping. This high targetability will be an asset to drug development, providing an opportunity for optimization and avoidance of toxicity that any one ASO might exhibit. Work is ongoing to identify the clinical candidate ASO, a process that involves careful activity and toxicity screening in animals. We suspect that exon 5 may be particularly amenable to ASO-induced exon skipping because it is an alternatively spliced exon that is naturally skipped in a small percentage of *CLN3* mRNA.

Therapeutic strategies for CLN3 Batten disease must take into consideration the timing of treatment. Ideally, a therapeutic could be administered after symptoms emerge, when children are diagnosed. It is likely that, as has been found for other neurodegenerative diseases such as SMA, earlier treatment will improve therapeutic value[37], though benefit is clearly observed after disease onset[38,39]. We show that pre-symptomatic dosing of ASO can have a therapeutic benefit. It remains to be determined whether later treatment, after deficits appear, will be effective. If an effective therapy becomes clinically available, CLN3 Batten mutations may be included on newborn screening panels and in carrier testing, as occurred

Author Manuscript Author Manuscript Author Manuscript Author Manuscript

following the US Food and Drug Administration approval of ASO treatments for SMA and Duchenne muscular dystrophy[40], making pre-symptomatic treatment possible.

Disease-causing nonsense mutations and frame-shifting deletions that create premature termination codons and truncated proteins are often associated with severe forms of disease and are difficult to treat with current gene-modifying approaches. Our study shows that reading-frame correction can have therapeutic value and provides support for the pursuit of this type of approach for the treatment of other pathological conditions caused by truncating mutations.

Online content

Any methods, additional references, Nature Research reporting summaries, source data, extended data, supplementary information, acknowledgements, peer review information; details of author contributions and competing interests; and statements of data and code availability are available at https://doi.org/10.1038/s41591-020-0986-1.

Methods

Protein modeling.

The CLN3 protein structure was modeled using a number of protein prediction servers[41–47]. This modeling predicts 8 to 11 TMDs, which is more than earlier models that proposed 6 TMDs[48], but similar to a recently published study[49] that predicted 11 TMDs. A homology model of the CLN3 structure using the structure of the equilibrative nucleoside transporter (ENT1), which is encoded by *SLC29A1*, as a template, was generated by I-TASSER (https://zhanglab.ccmb.med.umich.edu/I-TASSER)[50,51]. A membrane topology map as predicted by TOPCONS was rendered using Protter (http://wlab.ethz.ch/protter)[52].

Plasmids.

CLN3 expression plasmids were constructed by reverse transcription of mRNA isolated from human fibroblast cell lines with WT CLN3, homozygous CLN3$^{\Delta ex7/8}$ cells or from homozygous CLN3$^{\Delta ex7/8}$ cells treated with ASO-28 to generate CLN3$^{\Delta ex5/7/8}$. CLN3 WT, CLN3$^{\Delta ex7/8}$ and CLN3$^{\Delta ex5/7/8}$ cDNA was amplified by PCR using Phire Hot Start II DNA polymerase (Thermo Fisher Scientific) and primers specific for *CLN3* exon 1 with a restriction enzyme cleavage site for XbaI (hCLN3ex1F-XbaI) and for *CLN3* exon 15 with a BamHI restriction enzyme site (hCLN3ex15R-BamHI). Primer sequences are provided in Supplementary Table 1. The resulting products were purified, digested with XbaI and BamHI, and ligated into similarly digested pTT3 plasmid using T4 DNA ligase (New England Biolabs) to generate pTT3-hCLN3, pTT3-hCLN3Δex78 and pTT3-hCLN3Δex578. All plasmids were sequenced to confirm construction.

Immunoblot analysis.

Cells were collected using a scraper in 1× phosphate-buffered saline (PBS) buffer and washed once with 1× PBS. Cell lysate was prepared using radioimmunoprecipitation assay (RIPA) buffer (Thermo Fisher Scientific) supplemented with 1× Halt Protease Inhibitor

Author Manuscript Author Manuscript Author Manuscript Author Manuscript

Cocktail, EDTA-Free (Life Technologies) and 1× Halt Phosphatase Inhibitor Cocktail (Life Technologies) and cleared by centrifugation at 10,000*g* for 10 min at 4 °C. Protein concentration was determined by Lowry DC protein assay (Bio-Rad Laboratories). Proteins (20–40 μg per lane) were separated by 4–12% sodium dodecyl sulfate-polyacrylamide gel electrophoresis (SDS–PAGE), transferred to 0.2 μm or 0.4 μm nitrocellulose or 0.2 μm polyvinylidene difluoride using standard methods and membranes were blocked in StartingBlock T20 (TBS) Blocking Buffer (Life Technologies). Primary antibodies against LC3B (1:1,000, ab48394; Abcam), Phospho-S6 Ribosomal Protein (Ser240/244) (1:1,000, 2215 S; Cell Signaling Technology) and p62 (1:1,000, GP62-C; Progen) were diluted in blocking solution and were incubated with membranes at 4 °C overnight. Horseradish peroxidase-conjugated (7074 S; Cell Signaling Technology) or infrared fluorophore-conjugated secondary antibodies (925–32411, 925–32211 and 925–68021; LI-COR) were diluted in blocking solution and incubated with membranes at room temperature for 1 h. Immunoblots were detected with the OdysseyCLx imager (LI-COR) or developed using the Dura Western Blotting Detection System (Pierce) and exposed to film for imaging. Protein quantification was performed using Image Studio (LI-COR) analysis software and band densities were normalized to α-tubulin (1:5,000, 11224–1-AP; Proteintech).

Cell culture, transfection and treatments.

HEK-293 cells were cultured in Dulbecco's Modified Eagle's medium (DMEM) supplemented with 10% FBS, streptomycin (0.1 mg ml^{-1}), and penicillin (100 U ml^{-1}) in a 37 °C incubator with 5% carbon dioxide, according to the protocols provided by the American Type Culture Collection. Cells were seeded at 50% confluency in 96-well plates, 6-well plates, or chamber slides 1 d prior to transfection. One μg of pTT3-hCLN3 WT, pTT3-hCLN3Δex78 or pTT3-hCLN3Δex578 was transiently transfected using Lipofectamine 3000 plus Opti-MEM (Thermo Fisher Scientific) and incubated with cells for 48 h prior to DMSO or AZD8055 (ref. [53]) (Selleck Chemicals) addition (for 20 h) or starvation (for 16 h).

Fibroblast cell cultures, derived from patients with CLN3 Batten disease who are homozygous for *CLN3*$^{\Delta ex7/8}$ (SP3.2.1, SP9.2.1 and SP19.2.1) and individuals heterozygous for *CLN3*$^{\Delta ex7/8}$ (SP19.1.1 and SP19.1.2) were provided by F. Porter and A. D. Do (National Institutes of Health (NIH)/National Institute of Child Health and Human Development (NICHD)). Cells were transfected with 100 nM of ASO-C or ASO-28 using Lipofectamine 3000 (Thermo Fisher Scientific) and then treated with AZD8055 and DMSO as described above.

Human fibroblast and mouse cell lines were grown in HyClone DMEM/high glucose medium supplemented with 10% FBS. Primary homozygous *Cln3*$^{\Delta ex7/8}$ mouse cells were propagated in culture following isolation. In brief, the brain from an embryo at approximately embryonic day 17 (E17) was minced, and incubated with trypsin for 15 min. The tissue was then plated in DMEM/high glucose medium supplemented with 10% FBS and penicillin (100 U ml^{-1})/streptomycin (100 μg ml^{-1}). Adherent cells were propagated for 10–15 passages prior to transfection. ASOs targeting exon 5 of mouse *Cln3* or human *CLN3* were individually transfected into a primary cell line from homozygous *Cln3*$^{\Delta ex7/8}$ embryos

Author Manuscript Author Manuscript Author Manuscript Author Manuscript

or fibroblasts from a heterozygous individual or a patient with CLN3 Batten disease, at a final concentration of 100 nM, or for the dose response from 0 nM to 200 nM. ASOs were transfected into cells using Lipofectamine 3000 Reagent (Thermo Fisher Scientific) according to the manufacturer's protocol. Cells were collected in TRIzol (Life Technologies) after 48 h and analyzed for exon skipping.

For experiments with puromycin treatment, fibroblasts from a patient with CLN3 Batten disease were transfected with 100 nM of ASO-C, ASO-20, or ASO-28 as described above. After 42 h, the cells were treated with 200 μg ml^{-1} puromycin or vehicle for 6 h then RNA was collected using TRIzol and analyzed by RT–PCR as described below.

Immunofluorescent staining and imaging.

The Premo Autophagy Tandem Sensor RFP-GFP-LC3B Kit (P36239; Invitrogen) was used to visualize autophagy and LysoTracker Deep Red (L12492; Invitrogen) was used to visualize lysosomes in cells according to the manufacturer's protocols. In brief, 24 h prior to imaging, Premo Autophagy Tandem Sensor RFP-GFP-LC3B was added directly to cells at a concentration of 2 μl per 10,000 cells (titer: ~1×10^8 viral particles per ml) or LysoTracker was added directly to cells and incubated at 37 °C for 2 h at a concentration of 50 nM prior to cell fixation. Cells were counterstained with Hoechst 33342 (H3570; Invitrogen) nuclear stain for 15 min at 37 °C. Following staining, cells were washed with 1× PBS and fixed with 4% paraformaldehyde for 0.5 h at room temperature. Images were acquired using a confocal microscope (Leica SP8) and were captured from randomly selected fields of view. Z-stacks were generated from images taken at ~0.1 μm depth per section, and 3D images were generated using Imaris software (Bitplane). Ten randomly selected fields of view containing 10–12 cells were selected. Quantification of surface-rendered localization and puncta in the cells was performed using Imaris software. Confocal images were analyzed by counting the total number of autophagic vesicles per cell and lysosomes per cell.

Antisense oligonucleotides.

Synthesis and purification of all ASOs were performed as previously described[54–56]. ASOs were uniformly modified with 2′-*O*-methoxyethyl sugars with a phosphorothioate backbone. Lyophilized ASOs were dissolved in sterile PBS without calcium or magnesium and sterilized through a 0.2 μm filter. ASO sequences are provided in Supplementary Table 1. A BLAST search with the ASO-26 target sequence against the mouse genome revealed no other perfect sequence matches. A genomic sequence complementary to 15 nucleotides of ASO-26 was analyzed for changes in splicing of the encoded pre-mRNA by RT–PCR and was found to have no effect on splicing of exons surrounding this potential off-target binding site (Extended Data Fig. 10). Similar analysis of ASO-C revealed no matches to genomic sequences. The ASOs were diluted to the desired concentration required for dosing mice in sterile 0.9% saline.

Mice.

All protocols met ethical standards for animal experimentation and were approved by the Institutional Animal Care and Use Committee of Rosalind Franklin University of Medicine and Science (RFUMS). *Cln3*$^{\Delta ex7/8}$ mice were obtained from The Jackson Laboratory

Author Manuscript Author Manuscript Author Manuscript Author Manuscript

(B6.129(Cg)-*Cln3*$^{tm1.1Mem}$/J, stock number 017895)[1]. TgCRND8 mice on a C3H/C57BL/6 background ((B6C3-Tg(APPSwInd)8Dwst) express a double mutant of the human APP695 gene (Swedish K670N,M671L and Indiana V717F) driven from a hamster prion promoter[34,57]. Heterozygous male TgCRND8 mice were bred to homozygous *Cln3*$^{\Delta ex7/8}$ female mice to generate TgCRND8/*Cln3*$^{\Delta ex7/8}$ mice homozygous or heterozygous for *Cln3*$^{\Delta ex7/8}$ and with or without the *hAPP* transgene. Animals were housed on a 12-h light:dark cycle at a constant temperature of 19 °C in a pathogen-free environment with up to 5 animals per cage and access to food and water ad libitum. Mice were bred at RFUMS and pups were weaned at P21, at which time they were genotyped by extraction of DNA from ear tissue using Red Extract-N-Amp (Sigma-Aldrich) followed by PCR with mouse WT, *Cln3*$^{\Delta ex7/8}$, and for TgCRND8 crossed mice, *hAPP* transgene primers (see Supplementary Table 1 for sequences).

For adult ICV injections, mice (~2 months old) were placed in a stereotaxic frame and anesthetized with 2% isoflurane delivered by nose cone. The scalp was shaved and disinfected and a small incision was made in the scalp. A 10-μl Hamilton microsyringe with a 26 G Huber point needle was used to penetrate the skull at 0.2 mm posterior and 1.0 mm lateral to the bregma. The needle was lowered to a depth of 3 mm and 10 μl of a 500 μg ASO solution was injected into the right lateral ventricle at a rate of 1 μl s^{-1}. After 5 min, the needle was slowly withdrawn and the incision was sutured. The mice were then allowed to recover from the anesthesia in their home cage.

For neonatal ICV injection, pups (P1–P2) were treated with 25 μg of ASO according to a published procedure[58]. In brief, ASOs were diluted in sterile 0.9% saline with 0.01% Fast Green FCF and 2.5 μl was injected into the left ventricle of cryo-anesthetized pups using a 33-gauge needle affixed to a glass Hamilton syringe about 2.5 mm anterior to the lambda suture and 1 mm lateral to the sagittal suture to a depth of 2 mm. Mice were euthanized and brain tissue was dissected on ice-cold PBS and flash frozen in liquid nitrogen or placed in TRIzol reagent for immediate RNA extraction.

RNA isolation and analysis.

RNA was collected in TRIzol reagent according to the manufacturer's protocol. Mouse tissue was isolated and flash frozen in liquid nitrogen. Frozen tissues were homogenized in TRIzol and RNA was isolated from the samples according to the manufacturer's protocol. GoScript reverse transcriptase (Promega) and oligo(dT) primers were used to reverse transcribe 1 μg of the RNA following the manufacturer's recommendations. Splicing was analyzed by radiolabeled PCR of the cDNA using GoTaq Green (Promega) supplemented with α-^{32}P-deoxycytidine triphosphate. For analysis of mouse-derived samples, primers for mouse-specific *Cln3* exon 4 forward and *Cln3* exon 10 reverse were used. The expected amplicon sizes were 533 bp (full-length), 316 bp (*Cln3*$^{\Delta ex7/8}$) and 236 bp (*Cln3*$^{\Delta ex5/7/8}$). For human cell-line samples, human-specific *CLN3* exon 4 forward (F) and human *CLN3* exon 9 (Ra) or 10 (Rb) reverse were used with expected sizes of 433 bp (full-length), 353 bp (*CLN3*$^{\Delta ex5}$), 216 bp (*CLN3*$^{\Delta ex7/8}$) and 136 bp (*CLN3*$^{\Delta ex5/7/8}$) using the exon 4–9 primer set and 563 bp (full-length), 346 bp (*CLN3*$^{\Delta ex7/8}$) and 266 bp (*CLN3*$^{\Delta ex5/7/8}$) using the exon 4–10 primer set (Supplementary Table 1). The PCR amplicons were separated on a 6% non-

Author Manuscript Author Manuscript Author Manuscript Author Manuscript

denaturing polyacrylamide gel. The band intensities were quantified using a Typhoon FLA 7000 phosphorimager (GE Healthcare).

Immunohistochemistry.

Animals were anesthetized with 100 mg ml^{-1} urethane and transcardially perfused with PBS. One hemi-brain was immersion-fixed in 4% paraformaldehyde for 48 h then placed in 30% sucrose and stored at 4 °C. Sagittal slices (50 μm) of tissue were made using a Leica SM 2010R microtome and were permeabilized in PBS with 0.1% Triton X-100, blocked with 4% goat serum in PBS for 2 h and incubated with primary antibodies against 2′-*O*-methoxyethyl ASOs (1:1,000; Ionis Pharmaceuticals, 13545) overnight at 4 °C. Slices were washed with PBS followed by a 2-h incubation at room temperature with an anti-rabbit secondary antibody (1:400; Alexa Fluor 488, Thermo Fisher Scientific, A11008). Slices were washed with PBS 3 times for 10 min and then counterstained with Hoechst nuclear stain (1:10,000; Thermo Fisher Scientific, 33342) for 10 min. The slices were mounted on slides with coverslips using Prolong Gold antifade medium (Invitrogen). For SCMAS and GFAP staining, three slices per animal were used. Slices were incubated in 1% hydrogen peroxide in TBS for 20 min and then washed in TBS three times and blocked in 15% species-specific normal serum for 30 min. Slices were incubated overnight at 4 °C with anti-SCMAS (1:500; Abcam, ab181243) or anti-GFAP (1:250; Dako/Agilent, Z033429–2) diluted in TBS-T + 10% goat serum. Tissue slices were washed in PBS and then incubated with anti-rabbit biotinylated secondary antibody (1:2,000; Vector Laboratories, BA-1000) diluted in TBS-T + 10% goat serum for 2 h, followed by washing and incubation with ABC reagent (Vector Laboratories) for 2 h and then washed and incubated in 0.05% 3,3′-diaminobenzidine (DAB) solution. Finally, slices were washed 3 times, mounted, and then immersed in xylene for 10 min and mounted in DPX mountant and dried overnight. ASO distribution was imaged using a Fluoview FV10i confocal microscope with a ×10 and ×60 oil objective (Olympus). For DAB staining, slides were scanned on a Leica DM6000B slide-scanning microscope at ×20 magnification. Images were then extracted from respective regions at 2,400 × 2,400 pixel dimensions for image threshold analysis using ImageJ. Specifically, individuals blinded to sample identity completed the immunostaining and tissue processing, as well as imaging and threshold quantitation. All images were automatically processed with a macro to provide blind automated analysis and normalization across all tissues. Threshold values and summary data from ImageJ and the sample key were again blindly imported into a database and queried for immunoreactivity values for each animal or group; data were subsequently sorted by group alone and imported into graphing software for statistical analysis. After image acquisition the code key was provided for unblinding and analysis.

Accelerating rotarod.

Motor coordination was assessed using a Rotamex-5 rotarod (Columbus Instruments) in six trials (two blocks of three trials with a three-hour rest period between blocks). The rotarod accelerated from 0–37 rpm over the course of 3 min (acceleration of 0.5 rpm every 2 s) in a manner similar to that described previously[59]. Mice were habituated during three trials of two runs each with a 15 min rest between each trial. Three hours after the final habituation

Author Manuscript Author Manuscript Author Manuscript Author Manuscript

trial, the same protocol was used to collect test data. The latency to fall was digitally recorded and the average of the test runs was used.

Vertical pole test.

Three days after rotarod testing, mice were tested on a vertical pole navigation task according to a published method[26]. Mice were placed head upward at the top of a metal threaded pole with a height of 39 cm and a diameter of 1.1 cm and the time to completely turn around on the pole to a downward position was recorded. The average time measured in four consecutive trials was calculated. If a mouse failed to complete the action or fell off the pole, the run was assigned a time of 60 s.

Survival census.

Cages were checked daily for dead animals, which were collected and genotyped if death occurred prior to weaning. In some cases, carcasses were not present due to presumed cannibalization, in which case the subject was eliminated from the study data. Statistical analysis of survival as a function of genetic background was carried out in specific cohorts. Analysis was limited to the first six months of life. The probability of survival was assessed by the Kaplan–Meier technique, which assesses the probability of survival at every occurrence of death. The comparisons of cumulative survival curves were performed using the Gehan–Breslow–Wilcoxon test to assess differences.

Quantification and statistical analysis.

Statistical analyses were performed using GraphPad Prism 8 software (GraphPad) when $n > 2$. All data are presented as means ± s.e.m. with the number of samples provided (distinct samples or mice (n) or images within a cell or tissue (n); not repeated measures). The specific statistical test used for each experiment is detailed in the figure legends and raw data and details of statistical analysis are provided in the Source Data.

Reporting Summary.

Further information on research design is available in the Nature Research Reporting Summary linked to this article.

Data availability

The authors declare that all data supporting the findings of this study are available within the paper and its extended data and supplementary information files. Source data are provided with this paper.

Author Manuscript Author Manuscript Author Manuscript Author Manuscript

Extended Data

a

Prediction Server	WT	Δ78	Δ578
CCTop	11	4	5
OCTOPUS	10	4	4
Philius	11	3	6
Phobius	9	3	5
PolyPhobius	10	3	6
SCAMPI2	8	0	5
SPOCTOPUS	11	3	4
TOPCONS	11	3	5

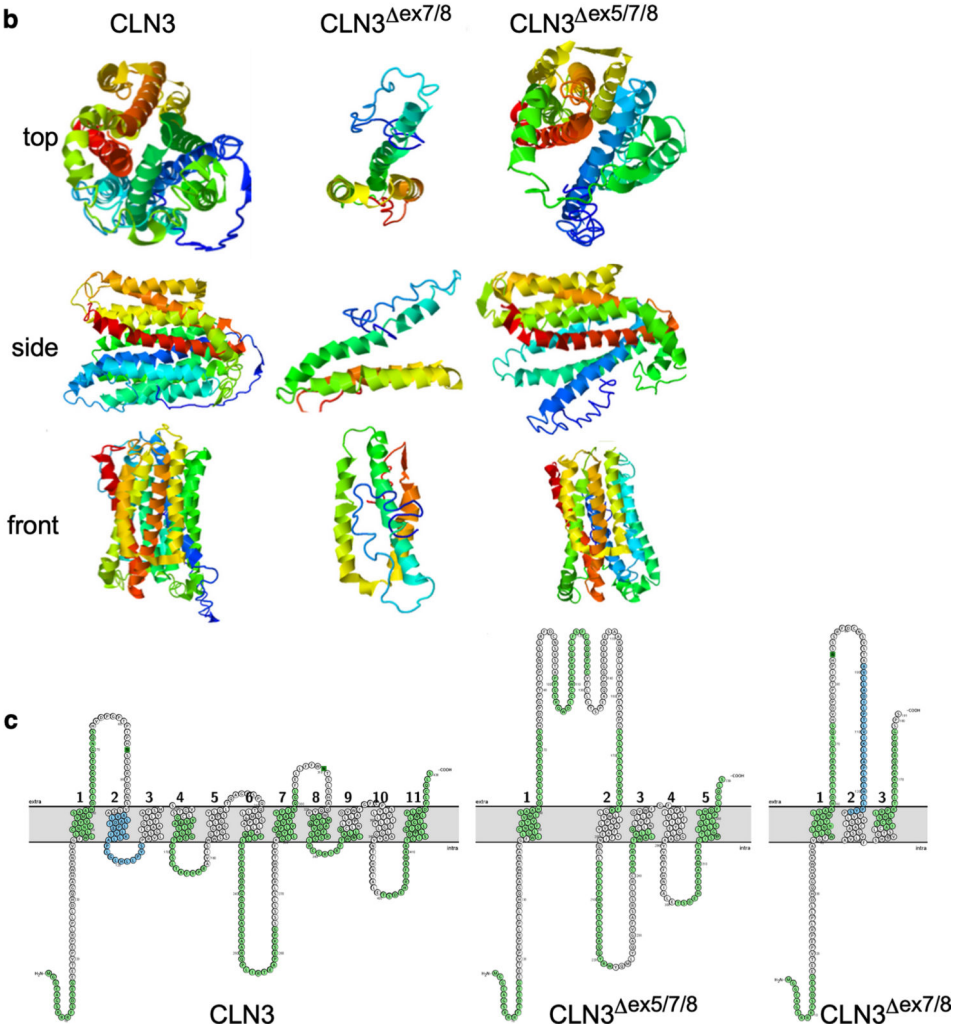

Extended Data Fig. 1 |. Modeling of CLN3 protein structure.

a, A query of the structures of CLN3 using different prediction algorithms, generated models of human CLN3. The table shows the protein prediction servers with their predicted number of transmembrane domains (TMDs) for CLN3 (WT), $CLN3^{\Delta ex7/8}$ (Δ78), and $CLN3^{\Delta ex5/7/8}$ (Δ578). The variability of TMDs amongst the different predictions demonstrates the uncertainty associated with such modeling approaches and cautions that

Author Manuscript Author Manuscript Author Manuscript Author Manuscript

definitive conclusions about CLN3 structures must await high resolution information on the structure from cryo-EM or X-ray crystallographic studies. **b**, Homology model of the CLN3 structure based on the structure of the equilibrative nucleoside transporter (ENT1) encoded by *SLC29A1*, as a template, generated by I-TASSER (https://zhanglab.ccmb.med.umich.edu/I-TASSER/). **c**, Membrane topology map of CLN3, $CLN3^{\Delta ex7/8}$ (Δ78), and $CLN3^{\Delta ex5/7/8}$ (Δ578) showing the numbered TMDs as predicted by TOPCONS and rendered using Protter (http://wlab.ethz.ch/protter). The exons corresponding to the amino acid sequence are shown in alternating green and white with exon 5-encoded amino acids highlighted in blue.

Author Manuscript Author Manuscript Author Manuscript Author Manuscript

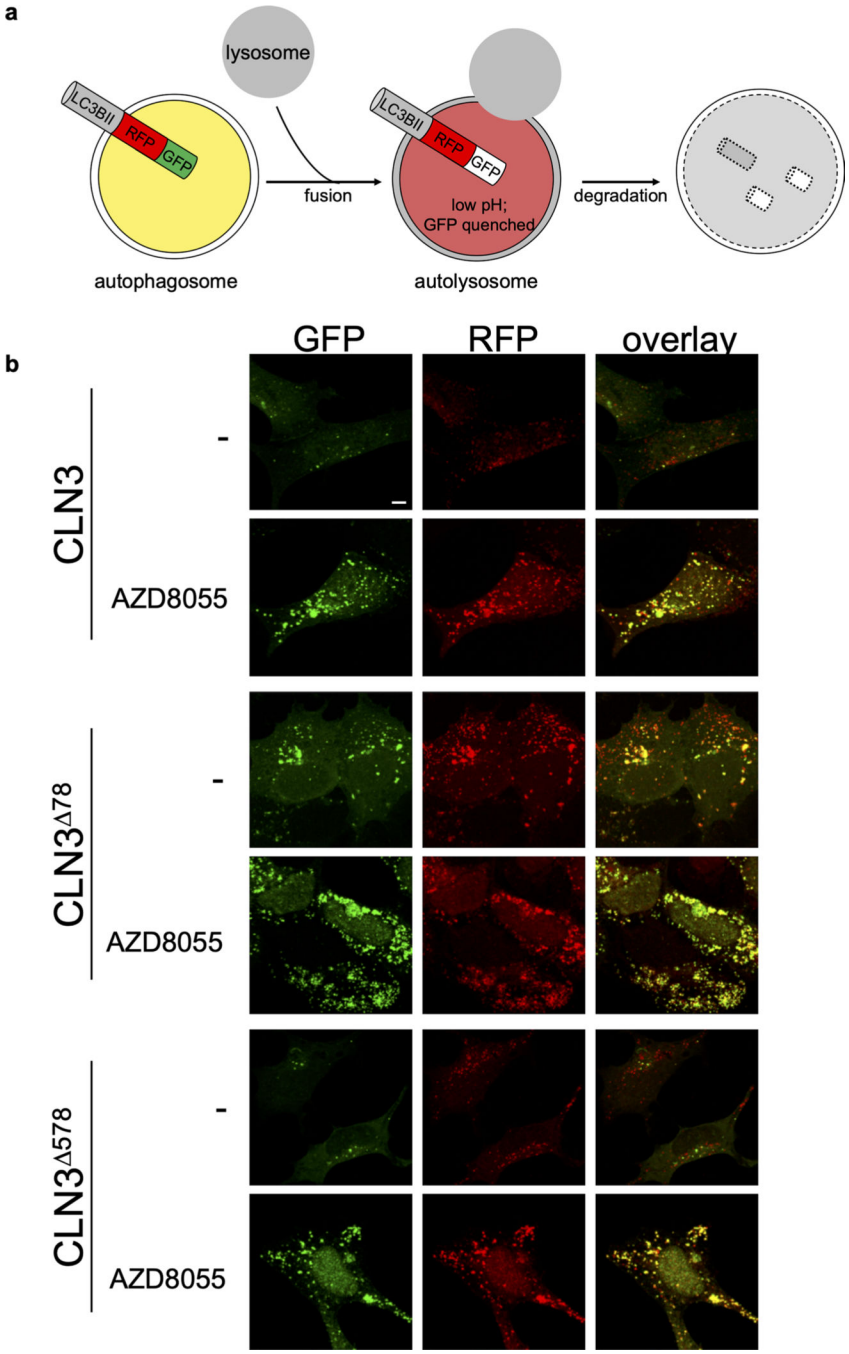

Extended Data Fig. 2 |. Autophagic flux deficits associated with CLN3$^{\Delta ex7/8}$ but not CLN3$^{\Delta ex5/7/8}$ expression.

a, Schematic representation of measuring autophagic flux using GFP-RFP-LC3B. to compare the effects of CLN3 protein isoforms on autophagic flux we used a tandem acid-stable red and acid-labile green fluorescent protein (RFP, GFP) sensor fused to the autophagosome-associated protein, microtubule-associated protein light chain 3 beta (GFP-RFP-LC3B) in HEK-293 cells. The GFP signal is quenched in acidic condition and thereby the dual-labeled RFP-GFP-LC3B provides a means to differentiate between

Author Manuscript Author Manuscript Author Manuscript Author Manuscript

autophagosomes (red and green=yellow fluorescent LC3B) and acidic autolysosomes (red only) and assess the relative abundance of the vesicles during autophagy. LC3BII localizes to the membrane of the autophagosome, which fuses with lysosomes to form acidic autolysosomes. This acidic environment causes quenching of the GFP making the autolysosome appear red. The contents, including RFP-LC3B and p62 are then degraded by lysosomal enzymes. **b,** HEK-293 cells were transfected with CLN3 WT, *CLN3*$^{\Delta ex7/8}$ (Δ78), or *CLN3*$^{\Delta ex5/7/8}$ (Δ578) expression plasmids. After 44 h, the cells were transfected with the tandem reporter GFP-RFP-LC3 to examine autophagic flux. Cells were treated with DMSO (−) or to induce autophagy, AZD8055 for 20 h then imaged. Shown are representative confocal microcopy images of the formation of autophagosomes (yellow in overlay images) and autolysosomes (red in overlay images) as quantitated in Fig. 1d, n = 10 cells/group. Scale bar, 5 μm.

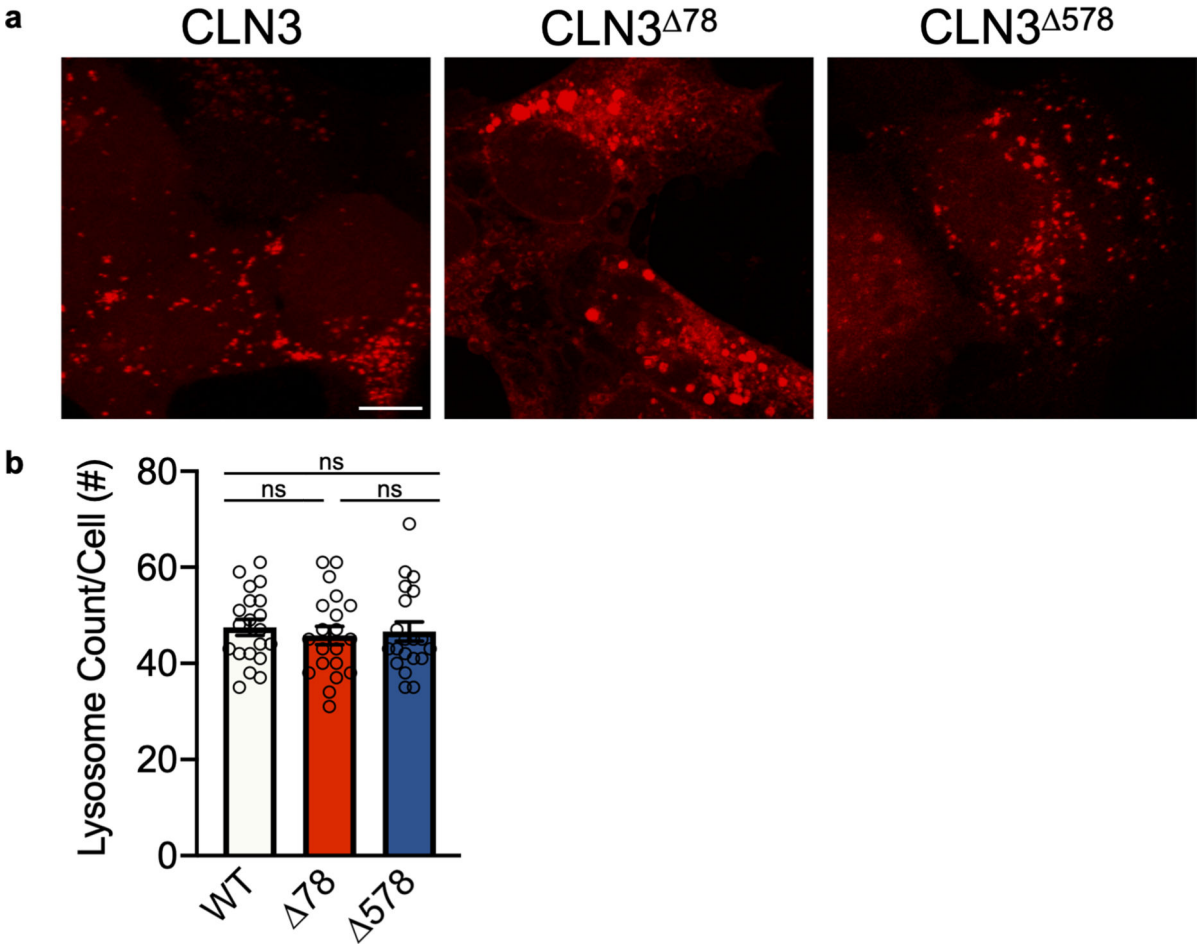

Extended Data Fig. 3 |. Lysosome assessment in cells expressing CLN3, CLN3$^{\Delta ex7/8}$, or CLN3$^{\Delta ex5/7/8}$.

a, Representative confocal microscopy images of HEK-293 cells expressing *CLN3 WT*, *CLN3*$^{\Delta ex7/8}$, or *CLN3*$^{\Delta ex5/7/8}$ and incubated with Lysotracker (red) to visualize lysosomes. Scale bar, 10 μm. **b**, The number of lysosomes per *CLN3 WT*, *CLN3*$^{\Delta ex7/8}$, or *CLN3*$^{\Delta ex5/7/8}$ expressing cells plotted as mean ± s.e.m. n = 20 cells per group. WT *CLN3* vs. *CLN3*$^{\Delta ex7/8}$,

P = 0.797; *CLN3*$^{\Delta ex7/8}$ vs. *CLN3*$^{\Delta ex5/7/8}$, P = 0.9447; WT *CLN3* vs. *CLN3*$^{\Delta ex5/7/8}$, P = 0.9447. One way ANOVA, Tukey's multiple comparisons test; Non-significant (ns).

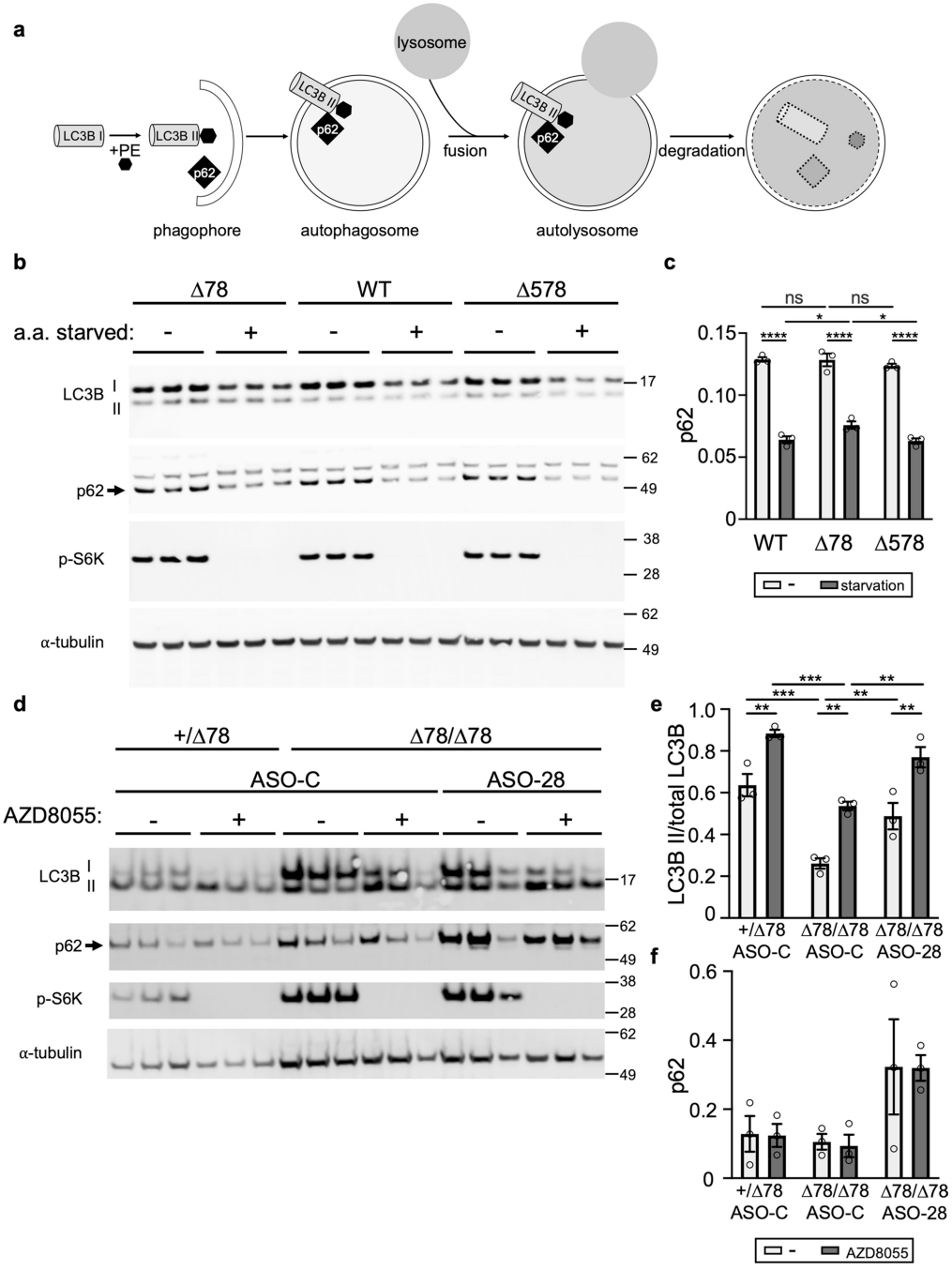

Extended Data Fig. 4 |. Normalization of autophagy measurements with CLN3$^{\Delta ex5/7/8}$ expression.

a, During the initiation of autophagy, LC3I undergoes lipidation and phosphatidylethanolamine (PE) conjugation to form LC3II which is engulfed in a newly formed phagophore with other cargo such as p62, which subsequently forms the autophagosome. Fusion with lysosomes results in formation of the autolysosomes followed

Author Manuscript Author Manuscript Author Manuscript Author Manuscript

Author Manuscript Author Manuscript Author Manuscript Author Manuscript

by degradation and recycling of resident contents. **b**, Western blot of protein lysate from HEK-293 cells transfected with *CLN3 WT*, *CLN3*$^{\Delta ex7/8}$ (Δ78), or *CLN3*$^{\Delta ex5/7/8}$ (Δ578) expression plasmids in the presence or absence of amino acids. Proteins were separated by SDS-PAGE and probed for LC3B, p62, and phospho-S6K, a marker of autophagy inhibition. α-tubulin was used as a loading control for each sample. Size markers (kilodaltons) are shown at right of gel images. **c**, Quantitation of p62 abundance relative to α-tubulin in **b**. Bars are mean ± s.e.m; $n = 3$ individually treated tissue culture wells per group. WT: fed vs. starvation, P < 0.0001; *CLN3*$^{\Delta ex7/8}$: fed vs. starvation, P < 0.0001; *CLN3*$^{\Delta ex5/7/8}$: fed vs. starvation, P < 0.0001; WT fed vs. *CLN3*$^{\Delta ex7/8}$ fed, P = 0.9999; *CLN3*$^{\Delta ex7/8}$ fed vs. *CLN3*$^{\Delta ex5/7/8}$ fed, P = 0.6193; WT fed vs. *CLN3*$^{\Delta ex5/7/8}$ fed, P = 0.5817; WT starvation vs. *CLN3*$^{\Delta ex7/8}$ starvation, P = 0.0497; *CLN3*$^{\Delta ex7/8}$ starvation vs. *CLN3*$^{\Delta ex5/7/8}$ starvation, P = 0.0324; WT starvation vs. *CLN3*$^{\Delta ex5/7/8}$ starvation, P = 0.9941. Two-way ANOVA, Sidak's multiple comparisons test; *P < 0.05, ****P < 0.0001, or non-significant (ns). **d**, Immunoblot detection of autophagy related proteins, LC3B, p62, and phospho-S6K in 3 different *CLN3*$^{+/\Delta ex7/8}$ and *CLN3*$^{\Delta ex7/8/\Delta ex7/8}$ human fibroblast cell lines treated with ASO-C or ASO-28 in the presence of absence of AZD8055-induced autophagy. Size markers (kilodaltons) are shown at right of gel images. **e**, Quantification of LC3B in **d**. $n = 3$ different CLN3$^{\Delta ex7/8}$ homozygous and $n = 3$ heterozygous cell lines. +/Δ78 ASO-C: vehicle vs. AZD8055, P = 0.0039; Δ78/Δ78 ASO-C: vehicle vs. AZD8055, P = 0.0017; Δ78/Δ78 ASO-28: vehicle vs. AZD8055, P = 0.0014; +/Δ78 ASO-C + vehicle vs. Δ78/Δ78 ASO-C + vehicle, P = 0.0001; Δ78/Δ78 ASO-C + vehicle vs. Δ78/Δ78 ASO-28 + vehicle, P = 0.0072; +/Δ78 ASO-C + vehicle vs. Δ78/Δ78 ASO-28 + vehicle, P = 0.0811; +/Δ78 ASO-C + AZD8055 vs. Δ78/Δ78 ASO-C + AZD8055, P = 0.0002; Δ78/Δ78 ASO-C + AZD8055 vs. Δ78/Δ78 ASO-28 + AZD8055, P = 0.0059; +/Δ78 ASO-C + AZD8055 vs. Δ78/Δ78 ASO-28 + AZD8055, P = 0.2210. Two-way ANOVA, Sidak's multiple comparisons test; **P < 0.01, ***P < 0.001. **f**, Densitometry analysis of p62 normalized to α-tubulin in **d**. Bars are mean ± s.e.m. $n = 3$ different CLN3$^{\Delta ex7/8}$ homozygous and $n = 3$ heterozygous cell lines. +/Δ78 ASO-C: vehicle vs. AZD8055, P > 0.9999.; Δ78/Δ78 ASO-C: vehicle vs. AZD8055, P = 0.9990; Δ78/Δ78 ASO-28: vehicle vs. AZD8055, P > 0.9999; +/Δ78 ASO-C + vehicle vs. Δ78/Δ78 ASO-C + vehicle, P = 0.9930; Δ78/Δ78 ASO-C + vehicle vs. Δ78/Δ78 ASO-28 + vehicle, P = 0.1074; +/Δ78 ASO-C + vehicle vs. Δ78/Δ78 ASO-28 + vehicle, P = 0.1641; +/Δ78 ASO-C + AZD8055 vs. Δ78/Δ78 ASO-C + AZD8055, P = 0.9841; Δ78/Δ78 ASO-C + AZD8055 vs. Δ78/Δ78 ASO-28 + AZD8055, P = 0.0908; +/Δ78 ASO-C + AZD8055 vs. Δ78/Δ78 ASO-28 + AZD8055, P = 0.1600. Two-way ANOVA, Sidak's multiple comparisons test; p > 0.05 for all comparisons.

Author Manuscript Author Manuscript Author Manuscript Author Manuscript

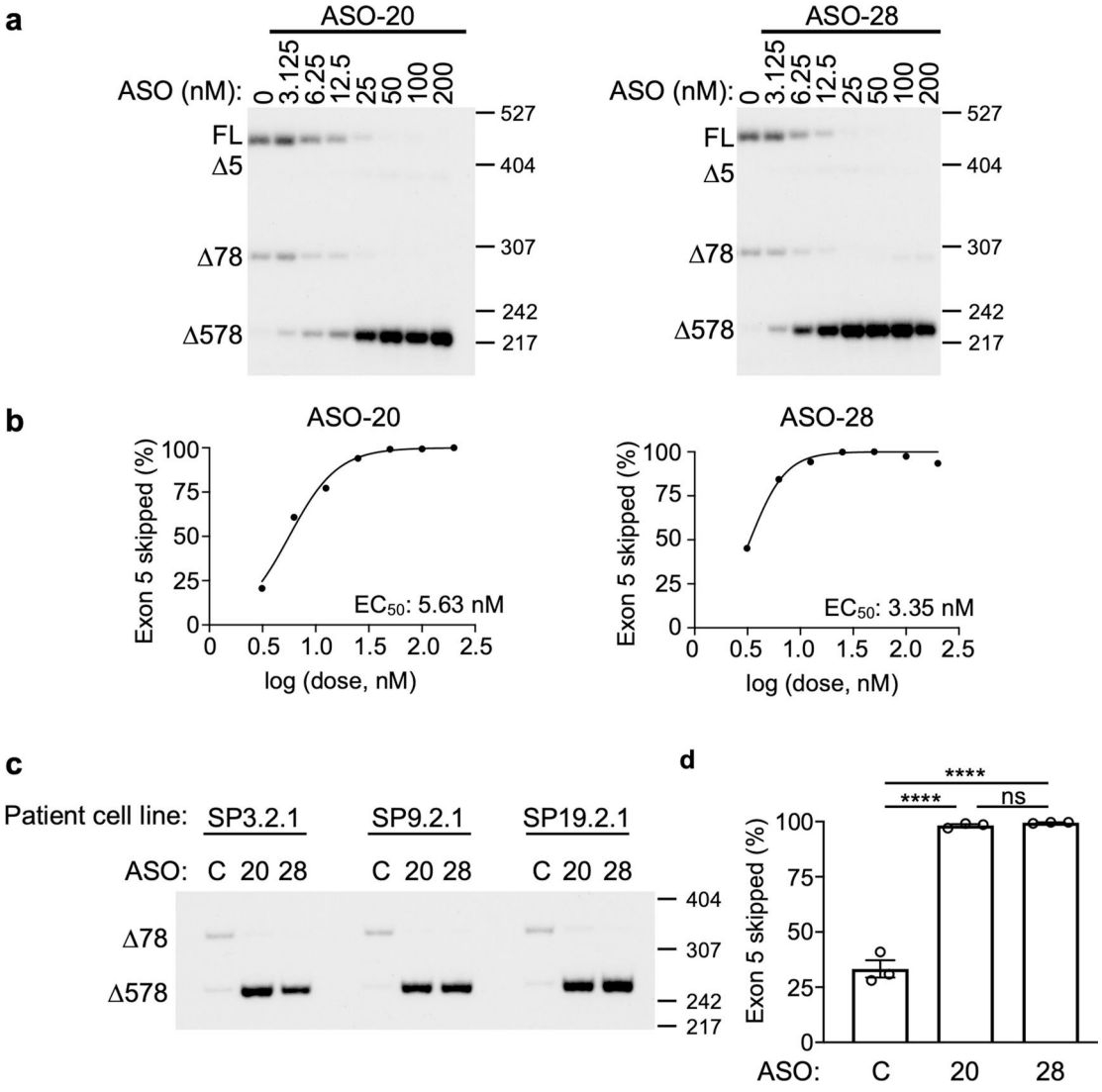

Extended Data Fig. 5 |. Dose-dependent exon 5 skipping with human *CLN3*-directed ASOs.
a, RT-PCR of RNA isolated from heterozygous *CLN3*$^{+/\Delta ex7/8}$ human fibroblast cell line treated with increasing concentrations (3.125 to 200 nM) of ASO-20 or ASO-28, as labeled. The spliced products are labeled at left of gel. Size markers (bp) are shown at right of gel. Quantitation of exon 5 skipping is shown as [Δ578/(Δ578 + Δ78)] × 100. Results reproduce ASO activity observed in homozygous *CLN3*$^{\Delta ex7/8}$ human fibroblast cell line shown in Fig. 1i. **b**, Exon 5 skipped (%) in relationship to the log of the dose is plotted. The half-maximal effective concentration (EC_{50}) was calculated after fitting the data using non-linear regression with a variable slope. **c**, RT-PCR analysis of exon 5 skipping in three different CLN3 Batten disease patient-derived cell lines homozygous for *CLN3*$^{\Delta ex7/8}$ transfected with the indicated ASOs. **d**, Quantification of the percentage of exon 5 skipped calculated as: [Δ578/(Δ578 + Δ78) × 100]. Bars are mean ± s.e.m. ASO-C (n = 3) vs. ASO-20 (n = 3), P < 0.0001; ASO-C vs. ASO-28 (n = 3), P < 0.0001; ASO-20 vs. ASO-26, P = 0.9216. One-way ANOVA with Tukey's multiple comparisons test; ****P < 0.0001, non-significant (ns). The spliced products are labeled at left of gel. Size markers (bp) are shown at right of gel.

Author Manuscript Author Manuscript Author Manuscript Author Manuscript

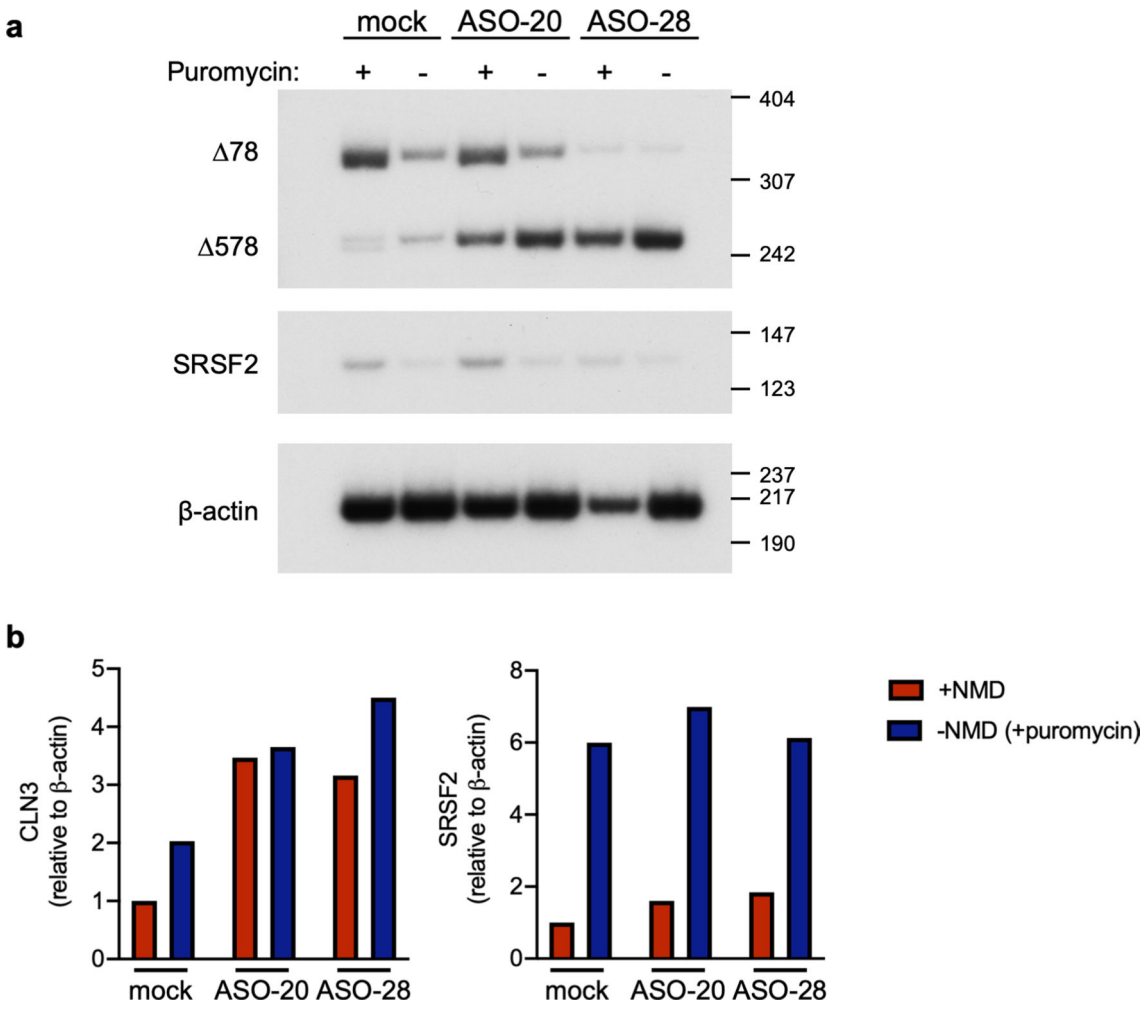

Extended Data Fig. 6 |. *CLN3*$^{\Delta ex7/8}$ mRNA is a substrate for nonsense-mediated decay.
a, RT-PCR analysis of *CLN3*$^{\Delta ex7/8}$ mRNA isolated from a CLN3 Batten disease patient fibroblast cell line transfected with the indicated ASOs and treated with puromycin to inhibit NMD (+) or left untreated (−). An *SRSF2* mRNA isoform (ENST00000452355.7) that is a known substrate for NMD was analyzed to confirm NMD inhibition with puromycin treatment. β-actin was included as a loading control. These results were reproduced in one additional independent experiment. **b**, Quantitation of total *CLN3* and SRSF2 mRNA in **a**. Size markers (basepairs) are shown at right of gel images.

Author Manuscript Author Manuscript Author Manuscript Author Manuscript

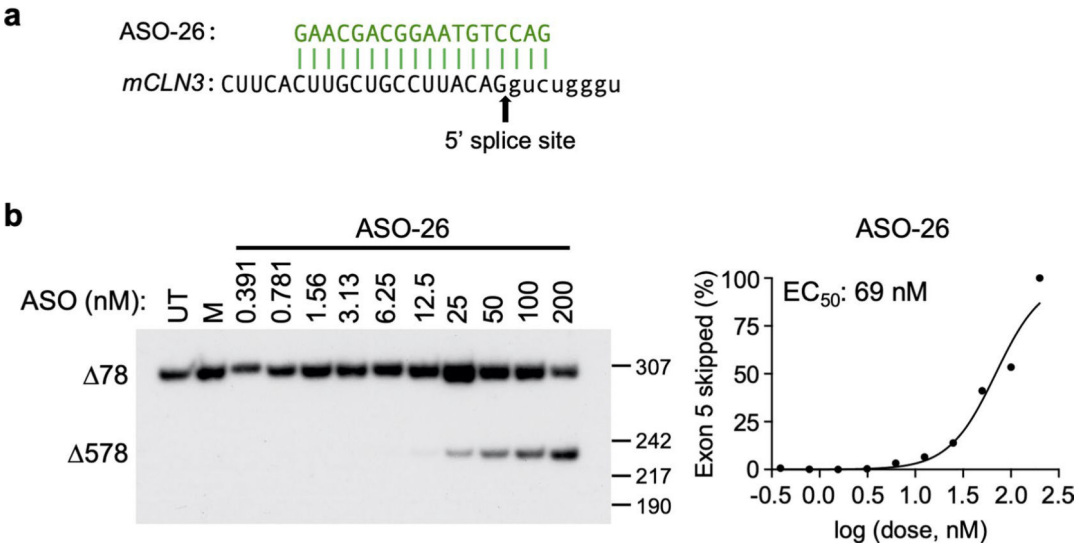

Extended Data Fig. 7 |. ASO dose-dependent exon 5 skipping in mouse cells.

a, Sequence alignment of the most active ASO to the target *Cln3* region. *Cln3* exonic and intronic nucleotides are displayed as capital and lowercase letters, respectively. **b**, RT-PCR analysis of exon 5 splicing from RNA extracted from homozygous *mCln3*$^{\Delta ex7/8}$ cells transfected with increasing concentrations of ASO-26 (0.391 nM to 200 nM). Spliced products are indicated at left of gel image and size markers (bp) are shown at right of gel. Graph shows results of a single experiment. Untreated (UT) and mock (M) treated controls are included. The graph displays the percent of exon 5 skipped [Δ578/(Δ578 + Δ78) × 100] in relationship to the log of the dose. The half-maximal effective concentration (EC_{50}) was calculated after fitting the data using nonlinear regression, variable slope.

Author Manuscript Author Manuscript Author Manuscript Author Manuscript

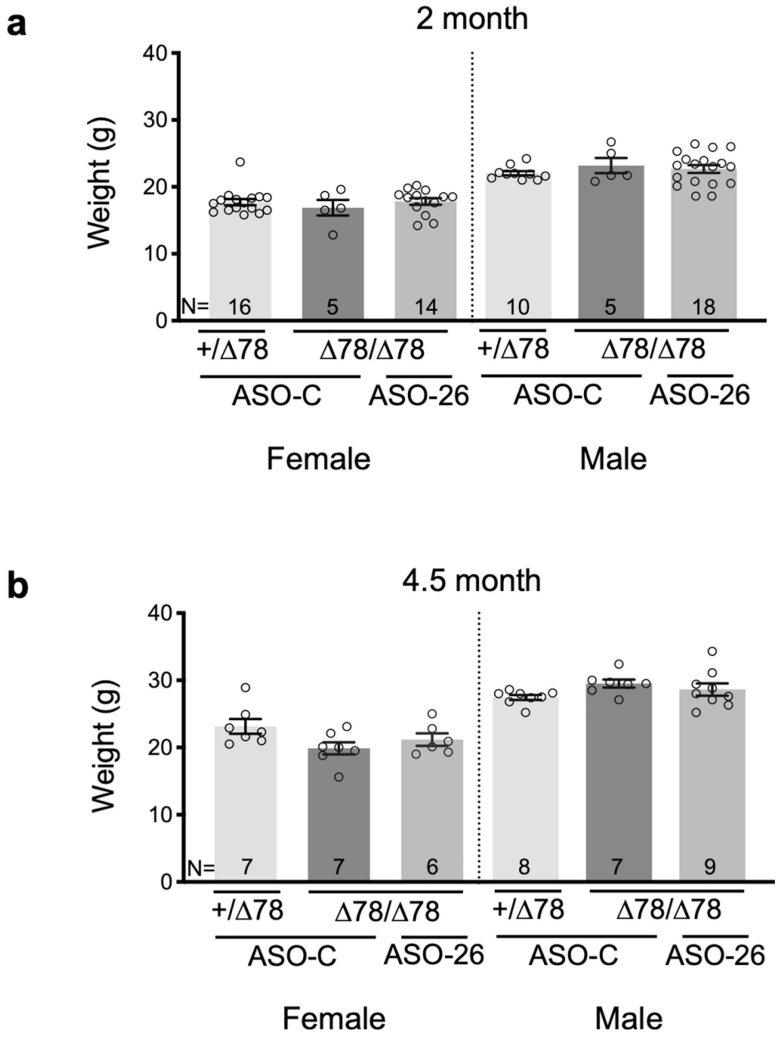

Extended Data Fig. 8 |. Mouse body weight following ASO-26 treatment.

Body weights of 2 month (**a**) and 4.5 month (**b**) old male and female *Cln3*$^{+/\Delta ex7/8}$ and *Cln3*$^{\Delta ex7/8/\Delta ex7/8}$ mice treated at P1–2 with ASO-C or ASO-26. Bars are mean ± s.e.m; *n* is shown in graph. 2 month females: +/Δ78 ASO-C vs. Δ78/Δ78 ASO-C, P = 0.6867; Δ78/Δ78 ASO-C vs. Δ78/Δ78 ASO-26, P = 0.9917; +/Δ78 ASO-C vs. Δ78/Δ78 ASO-26, P = 0.6420; 2 month males: +/Δ78 ASO-C vs. Δ78/Δ78 ASO-C, P = 0.59999; Δ78/Δ78 ASO-C vs. Δ78/Δ78 ASO-26, P = 0.8862; +/Δ78 ASO-C vs. Δ78/Δ78 ASO-26, P = 0.7368; 4.5 month females: +/Δ78 ASO-C vs. Δ78/Δ78 ASO-C, P = 0.0718; Δ78/Δ78 ASO-C vs. Δ78/Δ78 ASO-26, P = 0.6440; +/Δ78 ASO-C vs. Δ78/Δ78 ASO-26, P = 0.3740; 4.5 month males: +/Δ78 ASO-C vs. Δ78/Δ78 ASO-C, P = 0.1359; Δ78/Δ78 ASO-C vs. Δ78/Δ78 ASO-26, P = 0.6663; +/Δ78 ASO-C vs. Δ78/Δ78 ASO-26, P = 0.4463. One-way ANOVA, Tukey's multiple comparisons test. All comparisons were within sex and age groups; p > 0.05 for all comparisons.

Author Manuscript Author Manuscript Author Manuscript Author Manuscript

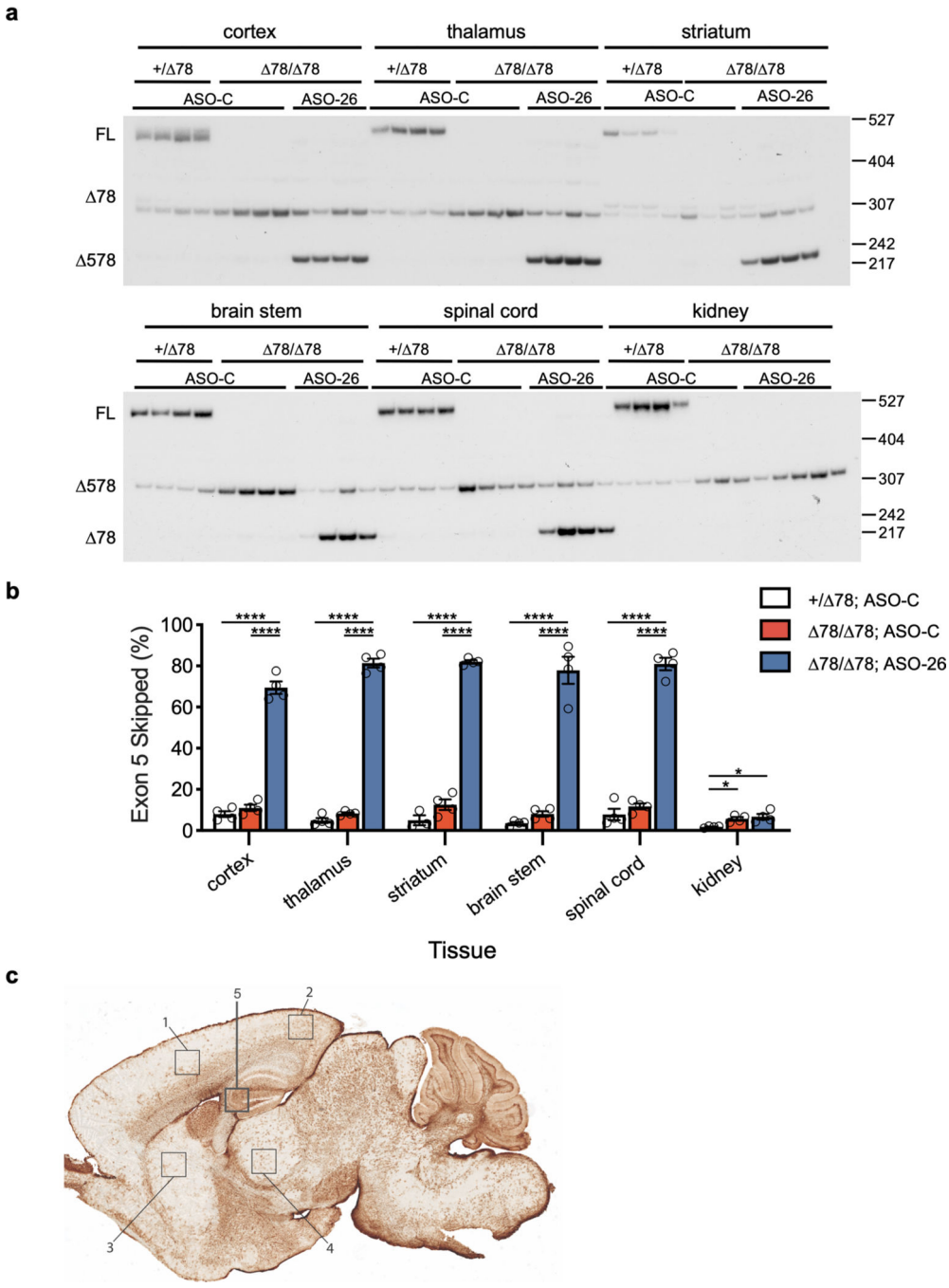

Extended Data Fig. 9 |. ASO activity in the CNS of ASO-treated mice.

a, RNA extracted from the cortex, thalamus, striatum, brain stem, spinal cord, and kidney of 19-week-old *Cln3*$^{+/\Delta ex7/8}$ (+/Δ78) and *Cln3*$^{\Delta ex7/8/\Delta ex7/8}$ (Δ78/Δ78) mice treated at P1 or P2 with ASO-C or ASO-26. **b**, Quantification of exon 5 skipping in (**a**). Bars are mean ± s.e.m. $n = 4$ for all but *Cln3*$^{+/\Delta ex7/8}$ ASO-C striatum $n = 3$; *P < 0.05, ****P < 0.0001, one-way ANOVA, Tukey's multiple comparisons test within each tissue. **c**, Brain map indicating regions sampled for SCMAS and GFAP immunohistochemistry. The regions numbered 1–5

Author Manuscript Author Manuscript Author Manuscript Author Manuscript

are the somatosensory cortex, visual cortex, striatum, thalamus, and hippocampus, respectively.

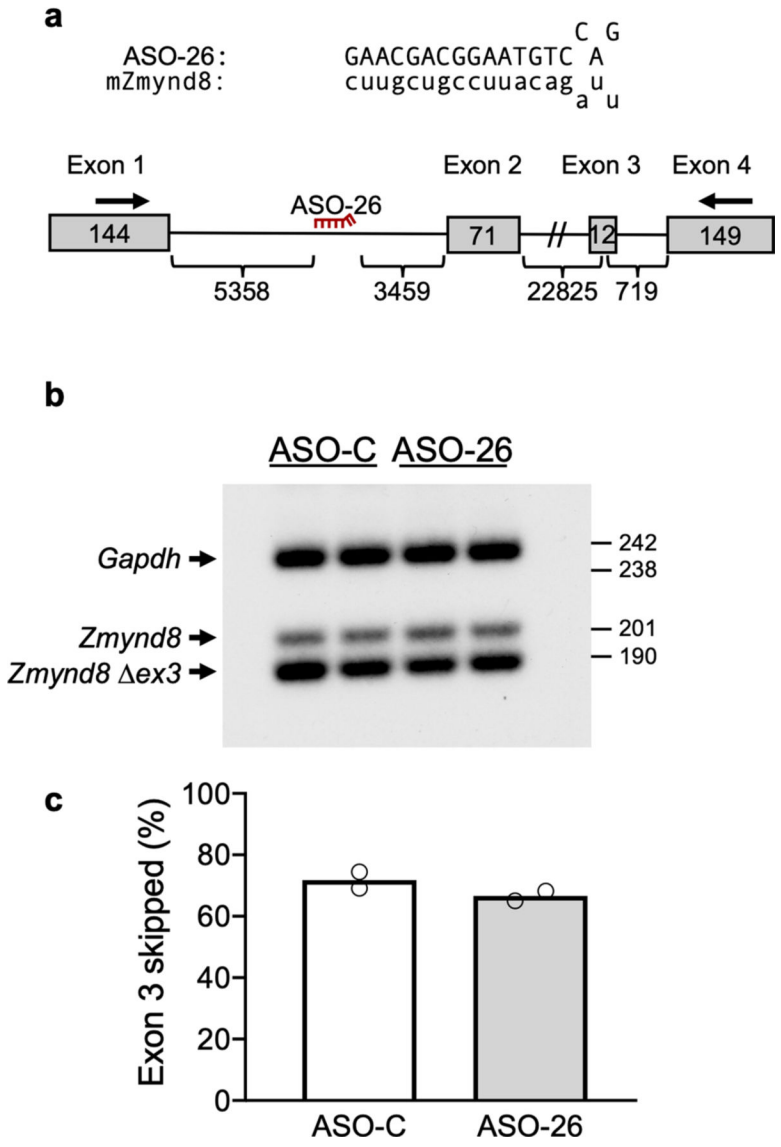

Extended Data Fig. 10 |. Assessing off-target activity of ASO-26.

a, The predicted ASO-26 binding location in *Zmynd8* pre-mRNA is shown. The arrows indicate the primer binding location. **b**, RT-PCR analysis of RNA extracted from the cortex of $Cln3^{\Delta ex7/8/\Delta ex7/8}$ mice treated with either ASO-C or ASO-26. The region of the *Zmynd8* transcript predicted to be affected by ASO-26 base pairing was amplified by RT-PCR and products were separated on a 6% polyacrylamide gel. Two alternatively spliced *Zmynd8* isoforms were detected at equal levels in all samples. RT-PCR of samples were analyzed twice with similar results. **c**, Quantification of exon 3 skipped shows that ASO-26 treatment does not alter *Zmynd8* alternative splicing. Bars are mean ± s.e.m. $n = 2$ mice.

Author Manuscript Author Manuscript Author Manuscript Author Manuscript

Supplementary Material

Refer to Web version on PubMed Central for supplementary material.

Acknowledgements

The authors thank Forbes Porter and An Dang Do (NIH/NICHD) and Beverly Davidson (Children's Hospital of Philadelphia) for human fibroblast cell lines and David Pearce (Sanford), David Mueller (RFUMS) and Susan Cotman (Harvard) for helpful discussions and other reagents. The authors also thank Maria Ruiz and Cecilia Reyes for technical support. This work was supported by NIH grant NS113233, the Batten Disease Support and Research Alliance and the ForeBatten Research Foundation. Quantitation of radioactive PCR products was performed on an instrument in the shared Proteomics facility at RFUMS obtained with NIH grant S10 OD010662.

References

1. Kyttala A, Ihrke G, Vesa J, Schell MJ & Luzio JP Two motifs target Batten disease protein CLN3 to lysosomes in transfected nonneuronal and neuronal cells. Mol. Biol. Cell 15, 1313–1323 (2004). [PubMed: 14699076]
2. The International Batten Disease Consortium Isolation of a novel gene underlying Batten disease, CLN3. Cell 82, 949–957 (1995). [PubMed: 7553855]
3. Cárcel-Trullols J, Kovács AD & Pearce DA Cell biology of the NCL proteins: what they do and don't do. Biochim. Biophys. Acta 1852, 2242–2255 (2015). [PubMed: 25962910]
4. Cialone J et al. Females experience a more severe disease course in Batten disease. J. Inherit. Metab. Dis. 35, 549–555 (2012). [PubMed: 22167274]
5. Gardiner RM Clinical features and molecular genetic basis of the neuronal ceroid lipofuscinoses. Adv. Neurol 89, 211–215 (2002). [PubMed: 11968447]
6. Johnson TB et al. Therapeutic landscape for Batten disease: current treatments and future prospects. Nat. Rev. Neurol 15, 161–178 (2019). [PubMed: 30783219]
7. Sleat DE, Gedvilaite E, Zhang Y, Lobel P & Xing J Analysis of large-scale whole exome sequencing data to determine the prevalence of genetically-distinct forms of neuronal ceroid lipofuscinosis. Gene 593, 284–291 (2016). [PubMed: 27553520]
8. Mole SE & Cotman SL Genetics of the neuronal ceroid lipofuscinoses (Batten disease). Biochim. Biophys. Acta 1852, 2237–2241 (2015). [PubMed: 26026925]
9. Kousi M, Lehesjoki AE & Mole SE Update of the mutation spectrum and clinical correlations of over 360 mutations in eight genes that underlie the neuronal ceroid lipofuscinoses. Hum. Mutat 33, 42–63 (2012). [PubMed: 21990111]
10. Wang F et al. Next generation sequencing-based molecular diagnosis of retinitis pigmentosa: identification of a novel genotype-phenotype correlation and clinical refinements. Hum. Genet 133, 331–345 (2014). [PubMed: 24154662]
11. Cao Y et al. Autophagy is disrupted in a knock-in mouse model of juvenile neuronal ceroid lipofuscinosis. J. Biol. Chem 281, 20483–20493 (2006). [PubMed: 16714284]
12. Chang JW, Choi H, Cotman SL & Jung YK Lithium rescues the impaired autophagy process in CbCln3(Δex7/8/Δex7/8) cerebellar cells and reduces neuronal vulnerability to cell death via IMPase inhibition. J. Neurochem 116, 659–668 (2011). [PubMed: 21175620]
13. Chandrachud U et al. Unbiased cell-based screening in a neuronal cell model of Batten disease highlights an interaction between $Ca2^{+}$ homeostasis, autophagy, and CLN3 protein function. J. Biol. Chem 290, 14361–14380 (2015). [PubMed: 25878248]
14. Vidal-Donet JM, Cárcel-Trullols J, Casanova B, Aguado C & Knecht E Alterations in ROS activity and lysosomal pH account for distinct patterns of macroautophagy in LINCL and JNCL fibroblasts. PLoS One 8, e55526 (2013). [PubMed: 23408996]
15. Yasa S et al. CLN3 regulates endosomal function by modulating Rab7A-effector interactions. J. Cell Sci. 133, jcs234047 (2020). [PubMed: 32034082]

Author Manuscript Author Manuscript Author Manuscript Author Manuscript

16. Kimura S, Noda T & Yoshimori T Dissection of the autophagosome maturation process by a novel reporter protein, tandem fluorescent-tagged LC3. Autophagy 3, 452–460 (2007). [PubMed: 17534139]
17. Klionsky DJ et al. Guidelines for the use and interpretation of assays for monitoring autophagy (3rd edition). Autophagy 12, 1–222 (2016). [PubMed: 26799652]
18. Havens MA & Hastings ML Splice-switching antisense oligonucleotides as therapeutic drugs. Nucleic Acids Res 44, 6549–6563 (2016). [PubMed: 27288447]
19. Cotman SL et al. Cln3(Δex7/8) knock-in mice with the common JNCL mutation exhibit progressive neurologic disease that begins before birth. Hum. Mol. Genet 11, 2709–2721 (2002). [PubMed: 12374761]
20. Tyynela J, Cooper JD, Khan MN, Shemilts SJ & Haltia M Hippocampal pathology in the human neuronal ceroid-lipofuscinoses: distinct patterns of storage deposition, neurodegeneration and glial activation. Brain Pathol 14, 349–357 (2004). [PubMed: 15605981]
21. Osorio NS et al. Neurodevelopmental delay in the *Cln3*Δex7/8 mouse model for Batten disease. Genes Brain Behav 8, 337–345 (2009). [PubMed: 19243453]
22. Pontikis CC et al. Late onset neurodegeneration in the $Cln3^{-/-}$ mouse model of juvenile neuronal ceroid lipofuscinosis is preceded by low level glial activation. Brain Res 1023, 231–242 (2004). [PubMed: 15374749]
23. Burkovetskaya M et al. Evidence for aberrant astrocyte hemichannel activity in juvenile neuronal ceroid lipofuscinosis (JNCL). PLoS One 9, e95023 (2014). [PubMed: 24736558]
24. Sondhi D et al. Partial correction of the CNS lysosomal storage defect in a mouse model of juvenile neuronal ceroid lipofuscinosis by neonatal CNS administration of an adeno-associated virus serotype rh.10 vector expressing the human *CLN3* gene. Hum. Gene Ther 25, 223–239 (2014). [PubMed: 24372003]
25. Aldrich A et al. Efficacy of phosphodiesterase-4 inhibitors in juvenile Batten disease (CLN3). Ann. Neurol 80, 909–923 (2016). [PubMed: 27804148]
26. Kovács AD & Pearce DA Finding the most appropriate mouse model of juvenile CLN3 (Batten) disease for therapeutic studies: the importance of genetic background and gender. Dis. Model Mech 8, 351–361 (2015). [PubMed: 26035843]
27. Wang X, Huang T, Bu G & Xu H Dysregulation of protein trafficking in neurodegeneration. Mol. Neurodegener 9, 31 (2014). [PubMed: 25152012]
28. Yang DS et al. Defective macroautophagic turnover of brain lipids in the TgCRND8 Alzheimer mouse model: prevention by correcting lysosomal proteolytic deficits. Brain 137, 3300–3318 (2014). [PubMed: 25270989]
29. Nilsson P et al. Aβ secretion and plaque formation depend on autophagy. Cell Rep 5, 61–69 (2013). [PubMed: 24095740]
30. Wisniewski KE, Kida E, Gordon-Majszak W & Saitoh T Altered amyloid β-protein precursor processing in brains of patients with neuronal ceroid lipofuscinosis. Neurosci. Lett 120, 94–96 (1990). [PubMed: 2127306]
31. Wisniewski KE, Gordon-Krajcer W & Kida E Abnormal processing of carboxy-terminal fragment of beta precursor protein (βPP) in neuronal ceroid-lipofuscinosis (NCL) cases. J. Inherit. Metab. Dis 16, 312–316 (1993). [PubMed: 8411989]
32. D'Andrea MR et al. Lipofuscin and Aβ42 exhibit distinct distribution patterns in normal and Alzheimer's disease brains. Neurosci. Lett 323, 45–49 (2002). [PubMed: 11911987]
33. Maulik M et al. Mutant human APP exacerbates pathology in a mouse model of NPC and its reversal by a β-cyclodextrin. Hum. Mol. Genet 21, 4857–4875 (2012). [PubMed: 22869680]
34. Chishti MA et al. Early-onset amyloid deposition and cognitive deficits in transgenic mice expressing a double mutant form of amyloid precursor protein 695. J. Biol. Chem 276, 21562–21570 (2001). [PubMed: 11279122]
35. Darras BT et al. An integrated safety analysis of infants and children with symptomatic spinal muscular atrophy (SMA) treated with Nnusinersen in seven clinical trials. CNS Drugs 33, 919–932 (2019). [PubMed: 31420846]
36. McClorey G & Wood MJ An overview of the clinical application of antisense oligonucleotides for RNA-targeting therapies. Curr. Opin. Pharm 24, 52–58 (2015).

Author Manuscript Author Manuscript Author Manuscript Author Manuscript

37. Foust KD et al. Rescue of the spinal muscular atrophy phenotype in a mouse model by early postnatal delivery of SMN. Nat. Biotechnol 28, 271–274 (2010). [PubMed: 20190738]
38. Dangouloff T & Servais L Clinical evidence supporting early treatment of patients with spinal muscular atrophy: current perspectives. Ther. Clin. Risk Manag 15, 1153–1161 (2019). [PubMed: 31632042]
39. De Vivo DC et al. Nusinersen initiated in infants during the presymptomatic stage of spinal muscular atrophy: interim efficacy and safety results from the Phase 2 NURTURE study. Neuromuscul. Disord 29, 842–856 (2019). [PubMed: 31704158]
40. Ke Q et al. Progress in treatment and newborn screening for Duchenne muscular dystrophy and spinal muscular atrophy. World J. Pediatr 15, 219–225 (2019). [PubMed: 30904991]

References

41. Viklund H & Elofsson A OCTOPUS: improving topology prediction by two-track ANN-based preference scores and an extended topological grammar. Bioinformatics 24, 1662–1668 (2008). [PubMed: 18474507]
42. Reynolds SM, Kall L, Riffle ME, Bilmes JA & Noble WS Transmembrane topology and signal peptide prediction using dynamic bayesian networks. PLoS Comput. Biol 4, e1000213 (2008). [PubMed: 18989393]
43. Kall L, Krogh A & Sonnhammer EL A combined transmembrane topology and signal peptide prediction method. J. Mol. Biol 338, 1027–1036 (2004). [PubMed: 15111065]
44. Kall L, Krogh A & Sonnhammer EL An HMM posterior decoder for sequence feature prediction that includes homology information. Bioinformatics 21, i251–i257 (2005). [PubMed: 15961464]
45. Bernsel A et al. Prediction of membrane-protein topology from first principles. Proc. Natl Acad. Sci. USA 105, 7177–7181 (2008). [PubMed: 18477697]
46. Viklund H, Bernsel A, Skwark M & Elofsson A SPOCTOPUS: a combined predictor of signal peptides and membrane protein topology. Bioinformatics 24, 2928–2929 (2008). [PubMed: 18945683]
47. Tsirigos KD, Peters C, Shu N, Kall L & Elofsson A The TOPCONS web server for consensus prediction of membrane protein topology and signal peptides. Nucleic Acids Res 43, W401–W407 (2015). [PubMed: 25969446]
48. Nugent T, Mole SE & Jones DT The transmembrane topology of Batten disease protein CLN3 determined by consensus computational prediction constrained by experimental data. FEBS Lett 582, 1019–1024 (2008). [PubMed: 18314010]
49. Perland E et al. Characteristics of 29 novel atypical solute carriers of major facilitator superfamily type: evolutionary conservation, predicted structure and neuronal co-expression. Open Biol 7, 170142 (2017). [PubMed: 28878041]
50. Yang J & Zhang Y I-TASSER server: new development for protein structure and function predictions. Nucleic Acids Res 43, W174–W181 (2015). [PubMed: 25883148]
51. Roy A, Kucukural A & Zhang Y I-TASSER: a unified platform for automated protein structure and function prediction. Nat. Protoc 5, 725–738 (2010). [PubMed: 20360767]
52. Omasits U, Ahrens CH, Muller S & Wollscheid B Protter: interactive protein feature visualization and integration with experimental proteomic data. Bioinformatics 30, 884–886 (2014). [PubMed: 24162465]
53. Chresta CM et al. AZD8055 is a potent, selective, and orally bioavailable ATP-competitive mammalian target of rapamycin kinase inhibitor with in vitro and in vivo antitumor activity. Cancer Res 70, 288–298 (2010). [PubMed: 20028854]
54. Swayze EE et al. Antisense oligonucleotides containing locked nucleic acid improve potency but cause significant hepatotoxicity in animals. Nucleic Acids Res 35, 687–700 (2007). [PubMed: 17182632]
55. Rigo F et al. Pharmacology of a central nervous system delivered 2′-*O*-methoxyethyl-modified survival of motor neuron splicing oligonucleotide in mice and nonhuman primates. J. Pharm. Exp. Ther 350, 46–55 (2014).

Author Manuscript Author Manuscript Author Manuscript Author Manuscript

56. Baker BF et al. 2′-*O*-(2-Methoxy)ethyl-modified anti-intercellular adhesion molecule 1 (ICAM-1) oligonucleotides selectively increase the ICAM-1 mRNA level and inhibit formation of the ICAM-1 translation initiation complex in human umbilical vein endothelial cells. J. Biol. Chem 272, 11994–12000 (1997). [PubMed: 9115264]

57. Hinrich AJ et al. Therapeutic correction of *ApoER2* splicing in Alzheimer's disease mice using antisense oligonucleotides. EMBO Mol. Med 8, 328–345 (2016). [PubMed: 26902204]

58. Hua Y & Krainer AR Antisense-mediated exon inclusion. Methods Mol. Biol 867, 307–323 (2012). [PubMed: 22454070]

59. Kovács AD et al. Temporary inhibition of AMPA receptors induces a prolonged improvement of motor performance in a mouse model of juvenile Batten disease. Neuropharmacology 60, 405–409 (2011). [PubMed: 20971125]

Author Manuscript Author Manuscript Author Manuscript Author Manuscript

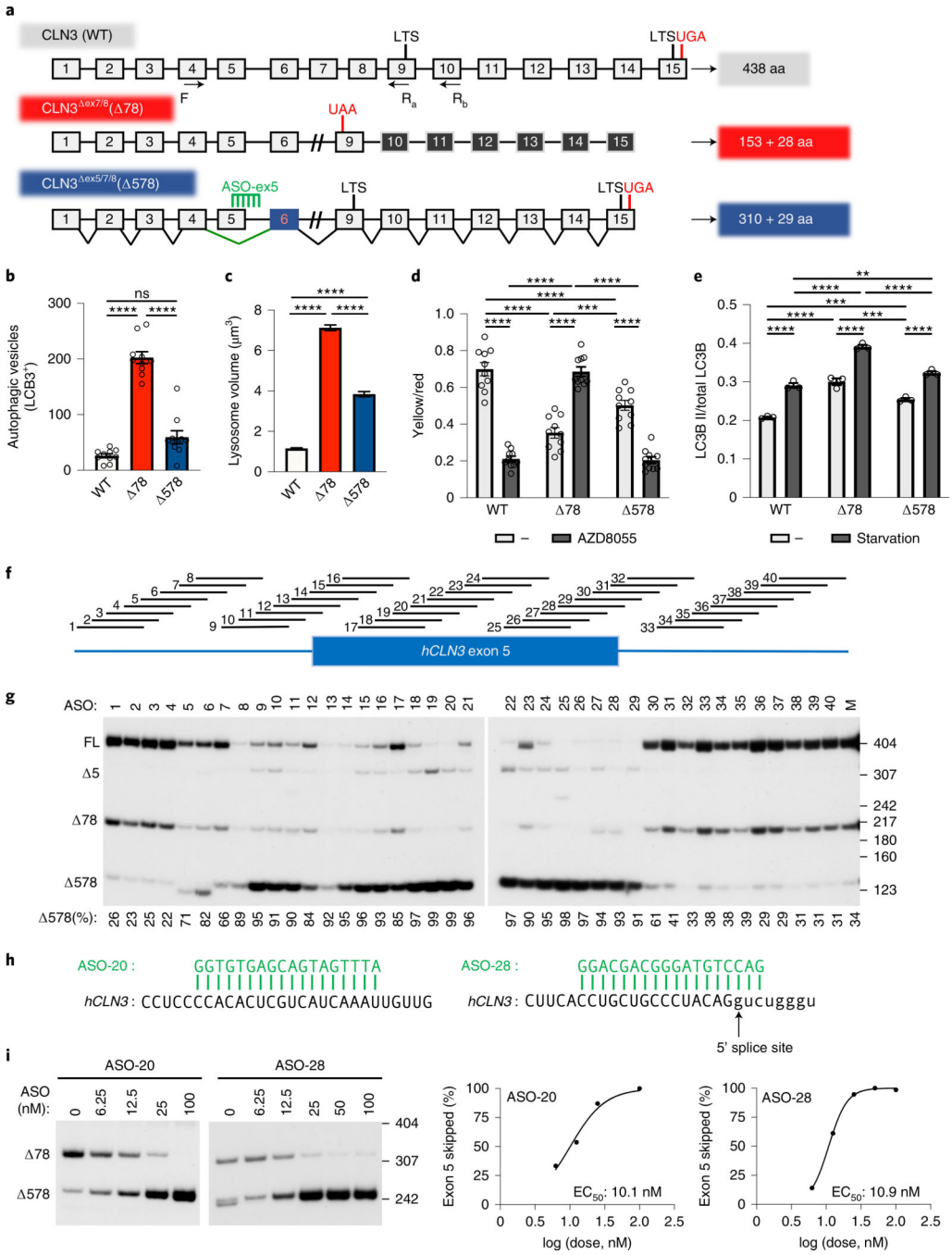

Fig. 1 |. ASO-induced exon 5 skipping to correct *CLN3*$^{\Delta ex7/8}$ reading frame and function.

a, *CLN3* (WT), *CLN3*$^{\Delta ex7/8}$ (Δ78), and the ASO-induced *CLN3*$^{\Delta ex5/7/8}$ (Δ578) spliced pre-mRNA isoforms. ASO-induced skipping of exon 5 in *CLN3*$^{\Delta ex7/8}$ corrects the reading frame and eliminates the premature termination codon (UAA). Amino acids in the protein products are shown including the 28 aa frame-shifted residues preceding the stop codon in CLN3$^{\Delta ex7/8}$ and the 29 frame-shifted aa in CLN3$^{\Delta ex5/7/8}$ prior to frame-correction in exon 9. Exons are depicted as boxes, introns as lines and splicing as diagonal lines. Stop codons and the regions encoding the LTS are labeled. The arrows indicate the location of the forward

Author Manuscript Author Manuscript Author Manuscript Author Manuscript

primer (F) targeting exon 4 and the reverse primers targeting exon 9 (R_a) and exon 10 (R_b) used in the RT–PCR analysis to detect the *CLN3* transcript. **b,** Elevated autophagic vesicles in cells expressing $CLN3^{\Delta ex7/8}$ but not WT *CLN3* or $CLN3^{\Delta ex5/7/8}$. Cells were cotransfected with the indicated expression plasmids and RFP-GFP-LC3 reagent and then evaluated by confocal microscopy (Extended Data Fig. 2). Total puncta per cell, indicative of RFP-GFP-LC3B in autophagosomes and autolysosomes were quantitated. Bars are mean ± s.e.m; n = 10 cells per group; (WT *CLN3* vs. $CLN3^{\Delta ex7/8}$, $P < 0.0001$; $CLN3^{\Delta ex7/8}$ vs. $CLN3^{\Delta ex5/7/8}$, $P < 0.0001$; WT *CLN3* vs. $CLN3^{\Delta ex5/7/8}$, $P = 0.0509$). One-way analysis of variance (ANOVA) with Sidak's multiple comparisons test; ****$P < 0.0001$ or non-significant (ns). **c**, Quantitation of lysosome volume in HEK-293 cells transfected with indicated *CLN3* WT, $CLN3^{\Delta ex7/8}$ or $CLN3^{\Delta ex5/7/8}$ expression plasmids and stained with LysoTracker to detect lysosomes (Extended Data Fig. 3). Bars are mean ± s.e.m. WT *CLN3* (n = 1,754 lysosomes) vs. $CLN3^{\Delta ex7/8}$ (n = 1,746 lysosomes), $P < 0.0001$; $CLN3^{\Delta ex7/8}$ vs. $CLN3^{\Delta ex5/7/8}$ (n = 1,058 lysosomes), $P < 0.0001$; WT *CLN3* vs. $CLN3^{\Delta ex5/7/8}$, $P < 0.0001$. One-way ANOVA with Sidak's multiple comparisons test; ****$P < 0.0001$. **d**, Defective autophagic flux in $CLN3^{\Delta ex7/8}$-expressing cells but not in *CLN3* WT or $CLN3^{\Delta ex5/7/8}$-expressing cells following AZD8055-induced autophagy. Cells were cotransfected with the indicated expression plasmids and RFP-GFP-LC3 and evaluated by confocal microscopy (Extended Data Fig. 2). Red and yellow (colocalized green and red) puncta were quantitated in the presence and absence of AZD8055. Bars are mean ± s.e.m; n = 10 cells per group. WT: vehicle vs. AZD8055, $P < 0.0001$; $CLN3^{\Delta ex7/8}$: vehicle vs. AZD8055, $P < 0.0001$; $CLN3^{\Delta ex5/7/8}$: vehicle vs. AZD8055, $P < 0.0001$; WT + vehicle vs. $CLN3^{\Delta ex7/8}$ + vehicle, $P < 0.0001$; $CLN3^{\Delta ex7/8}$ + vehicle vs. $CLN3^{\Delta ex5/7/8}$ + vehicle, $P = 0.0005$; WT + vehicle vs. $CLN3^{\Delta ex5/7/8}$ + vehicle, $P < 0.0001$; WT + AZD8055 vs. $CLN3^{\Delta ex7/8}$ + AZD8055, $P < 0.0001$; $CLN3^{\Delta ex7/8}$ + AZD8055 vs. $CLN3^{\Delta ex5/7/8}$ + AZD8055, $P < 0.0001$; WT + AZD8055 vs. $CLN3^{\Delta ex5/7/8}$ + AZD8055, $P = 0.9968$. Two-way ANOVA with Sidak's multiple comparisons test; ***$P < 0.001$ and ****$P < 0.0001$. **e**, Quantitation of immunoblot analysis (Extended Data Fig. 4) of LC3B in lysates from HEK-293 cells transfected with the indicated *CLN3* plasmids either fed (−) or starved of amino acids (starvation) to induce autophagy. Bars are mean ± s.e.m.; n = 3 individual treatment replicates per group. WT: fed vs. starvation, $P < 0.0001$; $CLN3^{\Delta ex7/8}$: fed vs. starvation, $P < 0.0001$; $CLN3^{\Delta ex5/7/8}$: fed vs. starvation, $P < 0.0001$; WT fed vs. $CLN3^{\Delta ex7/8}$ fed, $P < 0.0001$; $CLN3^{\Delta ex7/8}$ fed vs. $CLN3^{\Delta ex5/7/8}$ fed, $P = 0.0002$; WT fed vs. $CLN3^{\Delta ex5/7/8}$ fed, $P = 0.0002$; WT starvation vs. $CLN3^{\Delta ex7/8}$ starvation, $P < 0.0001$; $CLN3^{\Delta ex7/8}$ starvation vs. $CLN3^{\Delta ex5/7/8}$ starvation, $P < 0.0001$; WT starvation vs. $CLN3^{\Delta ex5/7/8}$ starvation, $P = 0.0032$. Two-way ANOVA, with Sidak's multiple comparisons test; **$P < 0.01$, ***$P < 0.001$ and ****$P < 0.0001$. **f**, Diagram of the location of ASOs 1 to 40 on the human *CLN3 (hCLN3)* exon 5 pre-mRNA. The blue box indicates exon 5 and the bars indicate the flanking introns. **g**, Radioactive RT–PCR using primers F and R_a (location shown in **a**) was performed on RNA extracted from $CLN3^{+/\Delta ex7/8}$ cells individually transfected with the indicated ASO. The spliced products are labeled on the left of the gel. Below: quantification of exon 5 splicing (as a percentage of total $CLN3^{\Delta ex7/8}$ mRNA) from a single experiment shown in the gel, calculated as: (Δ578/(Δ578 + Δ78)) × 100. A mock-treated control (M) is included. **h**, The nucleotide sequences of the optimal ASOs (green) aligned with the target *hCLN3* region. Exonic sequence is in capital letters and intronic sequence is in lower-case letters. **i**, RT–PCR analysis of the

region between primers F and R_b (shown in **a**), using RNA isolated from homozygous *CLN3*$^{\Delta ex7/8}$ cells treated with increasing doses of ASO-20 and ASO-28 (0 to 100 nM). The graphs (right) represent the percentage of exon 5 skipped in relation to the log of the dose from one experiment. Results of ASO activity were reproduced in a heterozygote cell line shown in Extended Data Fig. 5a. The ASO potency was determined by calculating the half-maximal effective concentration (EC_{50}) after fitting the data using nonlinear regression with a variable slope. Size markers (bp) are shown on the right of gel images.

Author Manuscript Author Manuscript Author Manuscript Author Manuscript

Author Manuscript Author Manuscript Author Manuscript Author Manuscript

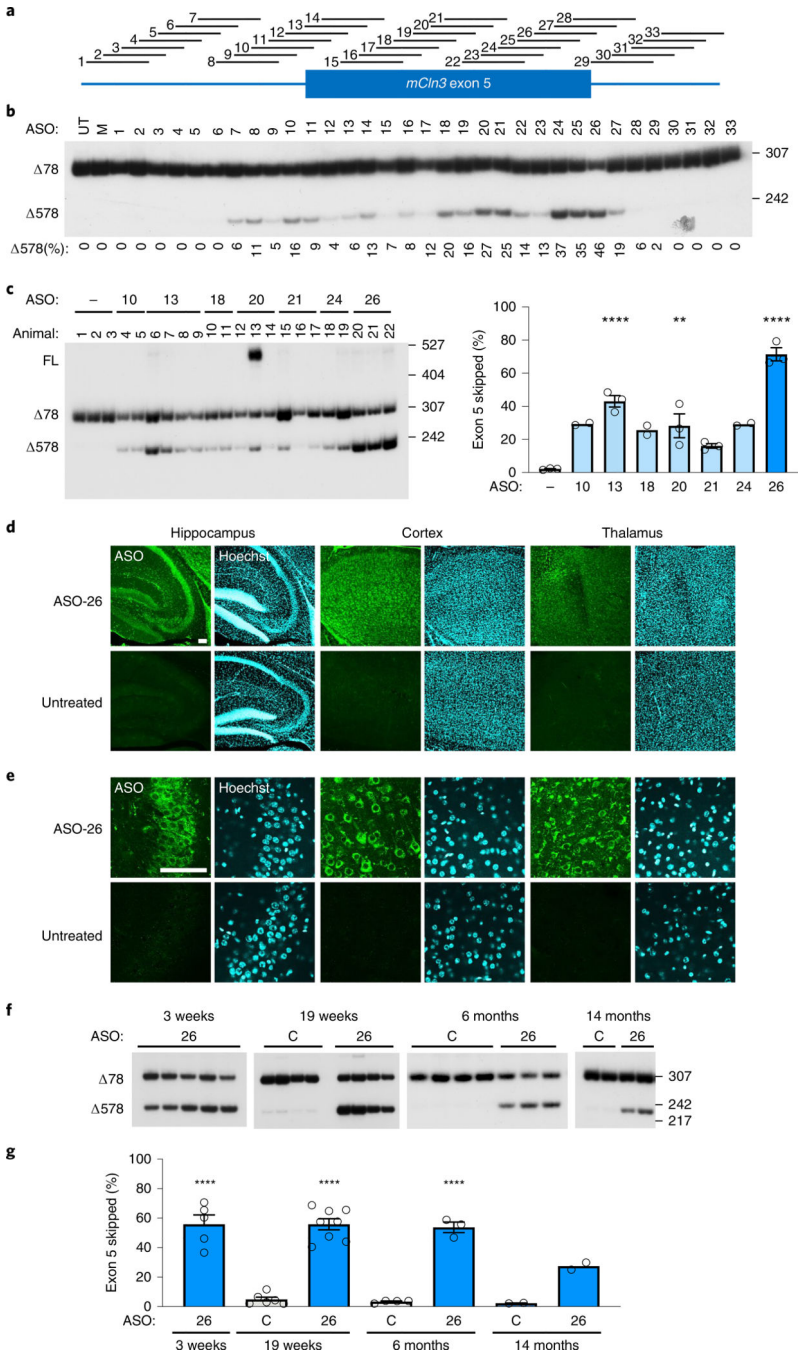

Fig. 2 |. ASOs induce long-lasting skipping of mouse *Cln3* exon 5 throughout the central nervous system.

a, Mapped location of the ASOs on mouse *Cln3* (*mCln3*) exon 5 pre-mRNA. The ASOs (horizontal lines) are numbered and overlap by 5 nt. The blue box represents *mCln3* exon 5 and the horizontal lines represent the flanking introns. **b**, RT–PCR of RNA from a homozygous $Cln3^{\Delta 7/8}$ mouse cell line individually transfected with the indicated ASO. The percentage of exon 5 skipped is indicated below the gel and was calculated as: (Δ578/(Δ578 + Δ78)) × 100. Untreated (UT) and mock (M) treated controls are included. This ASO activity screen was replicated in a WT *Cln3* mouse cell line. **c**, *Cln3* spliced products

Author Manuscript Author Manuscript Author Manuscript Author Manuscript

amplified from hippocampal cDNA made from RNA isolated from adult homozygous *Cln3*$^{\Delta ex7/8}$ mice two weeks after ICV treatment with PBS (−) or 500 μg of the indicated ASO (left). The graph (right) shows the quantification of the percentage of RT–PCR *Cln3*$^{\Delta ex5/7/8}$ product (Δ578/(Δ578 + Δ78)) × 100. Bars are mean ± s.e.m. One-way ANOVA with two-tailed Dunnett's multiple comparisons test to control-treated (−) samples (ASO-13, $n = 3$, $P < 0.0001$; ASO-20, $n = 3$, $P = 0.0035$; ASO-21, $n = 3$, $P = 0.1049$; ASO-26, $n = 3$, $P < 0.0001$). $^{**}P < 0.01$ and $^{****}P < 0.0001$. Animal no. 13 was genotyped as heterozygous, *Cln3*$^{+/\Delta ex7/8}$. **d**,**e**, Immunofluorescence staining of ASO (green) and the nuclear marker Hoechst (blue) in the hippocampus, somatosensory cortex (cortex) and thalamus at ×10 (**d**) and ×60 magnification (**e**) from 3-week-old homozygous *Cln3*$^{\Delta ex7/8}$ mice treated with 25 μg of ASO-26 at P1, and an untreated mouse. Scale bar, 100 μm. This experimental result was reproduced in 3 untreated and 7 ASO-26-treated mice analyzed at 4.5 months of age. **f**, RT–PCR analysis of exon 5 splicing in the hippocampus of heterozygous and homozygous *Cln3*$^{\Delta ex7/8}$ mice treated at P1 with ASO-26 or ASO-C and analyzed at 3 weeks, 19 weeks, 6 months and 14 months of age. **g**, Quantification of exon 5 skipping in groups shown in **f**. Details are as in **c** above; 3 weeks ASO-26 ($n = 5$) vs. 19 week ASO-C ($n = 6$) and 6 month ASO-C ($n = 4$), $P < 0.0001$; 19 week ASO-26 ($n = 8$) vs. 19 week ASO-C and 6 month ASO-C, $P < 0.0001$; 6 month ASO-26 ($n = 3$) vs. 19 week ASO-C and 6 month ASO-C, $P < 0.0001$. Bars are mean ± s.e.m. One-way ANOVA with two-tailed Dunnett's multiple comparisons to each ASO-C group; $^{****}P < 0.0001$. Size markers (bp) are shown on the right of gel images.

Author Manuscript Author Manuscript Author Manuscript Author Manuscript

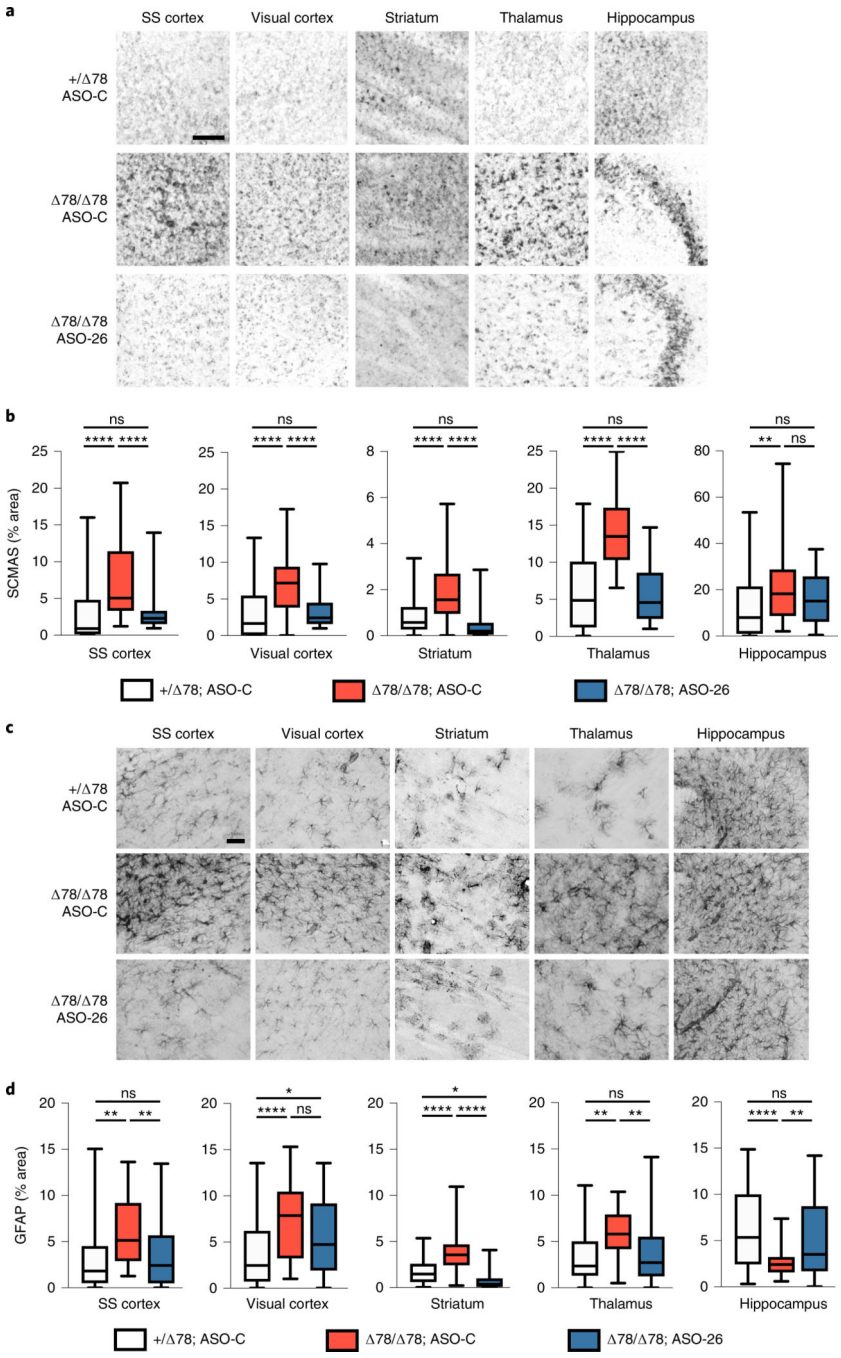

Fig. 3 |. ASO-26 treatment reduces subunit c of mitochondrial ATP synthase and GFAP in homozygous *Cln3*$^{\Delta ex7/8}$ mice.

a, Immunoreactivity of SCMAS in the somatosensory cortex (ss cortex), visual cortex, striatum, thalamus and hippocampus of 19-week-old heterozygous *Cln3*$^{\Delta ex7/8}$ mice (+/Δ78) treated with ASO-C and homozygous *Cln3*$^{\Delta ex7/8}$ mice (Δ78/Δ78) treated with ASO-C or ASO-26 at P1 or P2 (see Extended Data Fig. 9c for brain map indicating the regions sampled). Scale bar, 100 μm. **b**, Quantitative analysis of SCMAS in **a**. Center line, median; limits 25–75th percentile; whiskers, min–max. *n* = image fields per treatment group. SS

Author Manuscript Author Manuscript Author Manuscript Author Manuscript

cortex: +/Δ78 ASO-C (n = 56) vs. Δ78/Δ78 ASO-C (n = 56), P < 0.0001; Δ78/Δ78 ASO-C vs. Δ78/Δ78 ASO-26 (n = 36), P < 0.0001; +/Δ78 ASO-C vs. Δ78/Δ78 ASO-26, P = 0.9187. visual cortex + /Δ78 ASO-C (n = 56) vs. Δ78/Δ78 ASO-C (n = 56), P < 0.0001; Δ78/Δ78 ASO-C vs. Δ78/Δ78 ASO-26 (n = 36), P < 0.0001; +/Δ78 ASO-C vs. Δ78/Δ78 ASO-26, P = 0.8725; striatum: +/Δ78 ASO-C (n = 52) vs. Δ78/Δ78 ASO-C (n = 48), P < 0.0001; Δ78/Δ78 ASO-C vs. Δ78/Δ78 ASO-26 (n = 60), P < 0.0001; +/Δ78 ASO-C vs. Δ78/Δ78 ASO-26, P = 0.0743; thalamus + /Δ78 ASO-C (n = 56) vs. Δ78/Δ78 ASO-C (n = 56), P < 0.0001; Δ78/Δ78 ASO-C vs. Δ78/Δ78 ASO-26 (n = 32), P < 0.0001; +/Δ78 ASO-C vs. Δ78/Δ78 ASO-26, P = 0.8341; hippocampus: +/Δ78 ASO-C (n = 64) vs. Δ78/Δ78 ASO-C (n = 64), P = 0.0015; Δ78/Δ78 ASO-C vs. Δ78/Δ78 ASO-26 (n = 64), P = 0.0674; +/Δ78 ASO-C vs. Δ78/Δ78 ASO-26, P = 0.403. One-way ANOVA with Tukey's multiple comparisons test; ** P < 0.01, **** P < 0.0001 or non-significant (ns). **c**, Analysis of GFAP in the ss cortex, visual cortex, striatum, thalamus and hippocampus of 19 week-old *Cln3*$^{+/\Delta ex7/8}$ and *Cln3*$^{\Delta ex7/8/\Delta ex7/8}$ mice treated at P1 or P2 with either ASO-C or ASO-26. Scale bar, 100 μm. **d**, Quantitation of GFAP accumulation in the corresponding regions. Center line, median; limits 25–75th percentile; whiskers, min–max. n= image fields per treatment group. SS cortex: +/Δ78 ASO-C (n = 56) vs. Δ78/Δ78 ASO-C (n = 48), P = 0.0002; Δ78/Δ78 ASO-C vs. Δ78/Δ78 ASO-26 (n = 64), P = 0.0004; +/Δ78 ASO-C vs. Δ78/Δ78 ASO-26, P = 0.9648; visual cortex: + /Δ78 ASO-C (n = 56) vs. Δ78/Δ78 ASO-C (n = 48), P < 0.0001; Δ78/Δ78 ASO-C vs. Δ78/Δ78 ASO-26 (n = 64), P = 0.0644; +/Δ78 ASO-C vs. Δ78/Δ78 ASO-26, P = 0.0494; striatum: +/Δ78 ASO-C (n = 52) vs. Δ78/Δ78 ASO-C (n = 48), P < 0.0001; Δ78/Δ78 ASO-C vs. Δ78/Δ78 ASO-26 (n = 60), P < 0.0001; +/Δ78 ASO-C vs. Δ78/Δ78 ASO-26, P = 0.019; thalamus + /Δ78 ASO-C (n = 56) vs. Δ78/Δ78 ASO-C (n = 48), P = 0.0013; Δ78/Δ78 ASO-C vs. Δ78/Δ78 ASO-26 (n = 64), P = 0.0048; +/Δ78 ASO-C vs. Δ78/Δ78 ASO-26, P = 0.8634; hippocampus: +/Δ78 ASO-C (n = 44) vs. Δ78/Δ78 ASO-C (n = 48), P < 0.0001; Δ78/Δ78 ASO-C vs. Δ78/Δ78 ASO-26 (n = 56), P = 0.0023; +/Δ78 ASO-C vs. Δ78/Δ78 ASO-26, P = 0.3118. One-way ANOVA with Tukey's multiple comparisons test; * P < 0.05, ** P < 0.01; *** P < 0.001, **** P < 0.0001 or non-significant (ns).

Author Manuscript Author Manuscript Author Manuscript Author Manuscript

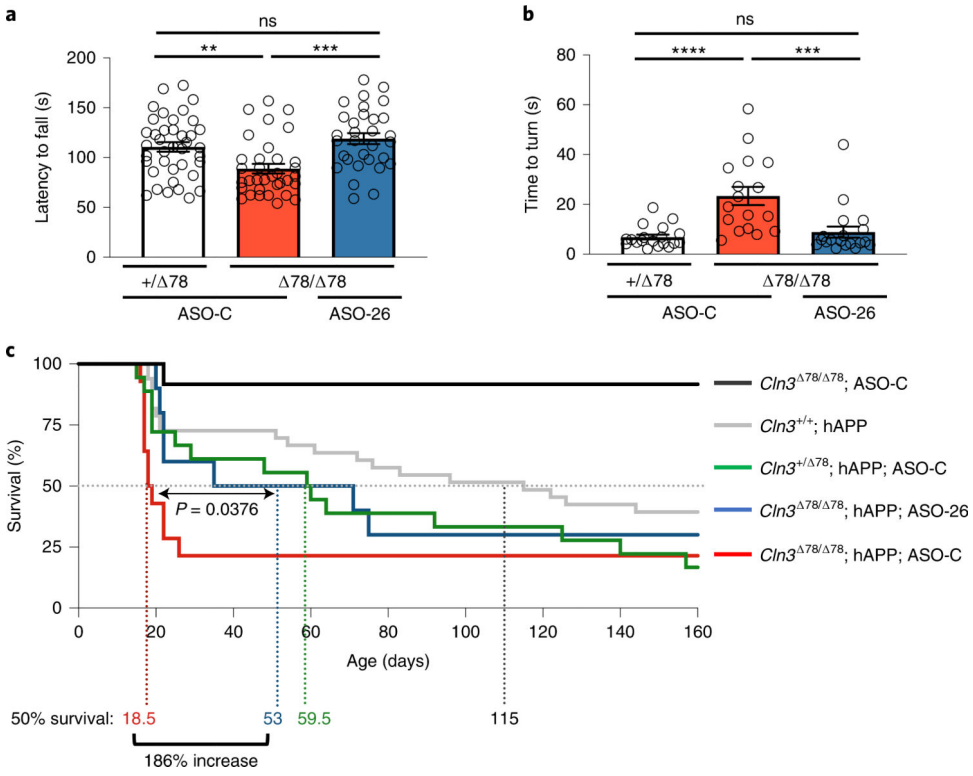

Fig. 4 |. Improved motor coordination and survival in CLN3 Batten mouse models following ASO-26 treatment.

(**a**) *Cln3*$^{+/\Delta ex7/8}$ and *Cln3*$^{\Delta ex7/8/\Delta ex7/8}$ mice treated with ASO-C or ASO-26 at P1 or P2 were assessed for motor activity on an accelerating rotarod at two months of age. The latency to fall on the accelerating rotarod is plotted as mean ± s.e.m. *n* = number of individual mice. *Cln3*$^{+/\Delta ex7/8}$ ASO-C (*n* = 39) vs. *Cln3*$^{\Delta ex7/8/\Delta ex7/8}$ ASO-C (*n* = 34), *P* = 0.0062; *Cln3*$^{\Delta ex7/8/\Delta ex7/8}$ ASO-C vs. *Cln3*$^{\Delta ex7/8/\Delta ex7/8}$ ASO-26 (*n* = 31), *P* = 0.0002; *Cln3*$^{+/\Delta ex7/8}$ ASO-C vs. *Cln3*$^{\Delta ex7/8/\Delta ex7/8}$ ASO-26, *P* = 0.4719. One-way ANOVA with Tukey's multiple comparisons test; $^{**}P < 0.01$, $^{***}P < 0.001$ or non-significant (ns). **b**, Vertical pole test to assess motor coordination. The average time to turn downward 180° on a vertical pole is plotted as mean ± s.e.m. *n* = number of individual mice. *Cln3*$^{+/\Delta ex7/8}$ ASO-C (*n* = 19) vs. *Cln3*$^{\Delta ex7/8/\Delta ex7/8}$ ASO-C (*n* = 17), *P* < 0.0001; *Cln3*$^{\Delta ex7/8/\Delta ex7/8}$ ASO-C vs. *Cln3*$^{\Delta ex7/8/\Delta ex7/8}$ ASO-26 (*n* = 19), *P* = 0.0004; *Cln3*$^{+/\Delta ex7/8}$ ASO-C vs. *Cln3*$^{\Delta ex7/8/\Delta ex7/8}$ ASO-26, *P* = 0.8238. One-way ANOVA with Tukey's multiple comparisons test; $^{***}P < 0.001$, $^{****}P < 0.0001$ or non-significant (ns). **c**, Kaplan–Meier curves for survival, *P* < 0.0001, two-tailed, Gehan–Breslow–Wilcoxon test. Curve comparison for ASO-C (*n* = 14) vs. ASO-26 (*n* = 10) treated *Cln3*$^{\Delta ex7/8/\Delta ex7/8}$; hAPP mice, *P* = 0.0376, two-tailed, Gehan–Breslow–Wilcoxon test. *Cln3*$^{\Delta ex7/8/\Delta ex7/8}$; ASO-C (*n* = 12), *Cln3*$^{+/+}$; hAPP (*n* = 33), *Cln3*$^{+/\Delta ex7/8}$; hAPP; ASO-C (*n* = 18). *n* = number of individual mice.